Master's thesis
Meteorology

The effect of street vegetation configuration on the pedestrian-level aerosol mass concentrations in a wide street canyon

Sasu Karttunen

May 16, 2020

Supervisors: M.Sc. Mona Kurppa
Assoc. prof. Leena Järvi

Censors: Prof. Heikki Järvinen
Assoc. prof. Leena Järvi

UNIVERSITY OF HELSINKI
Master's Programme in Atmospheric Sciences

P.O. Box 64 (Gustaf Hällströmin katu 2)
FI-00014 University of Helsinki

HELSINGIN YLIOPISTO — HELSINGFORS UNIVERSITET — UNIVERSITY OF HELSINKI

Tiedekunta — Fakultet — Faculty	Koulutusohjelma — Utbildningsprogram — Education programme
Faculty of Science	Master's Programme in Atmospheric Sciences

Tekijä — Författare — Author
Sasu Karttunen

Työn nimi — Arbetets titel — Title
The effect of street vegetation configuration on the pedestrian-level aerosol mass concentrations in a wide street canyon

Pääaine — Huvudämne — Major
Meteorology

Työn laji — Arbetets art — Level	Aika — Datum — Date	Sivumäärä — Sidoantal — Number of pages
Master's thesis	May 16, 2020	59 pages

Tiivistelmä — Referat — Abstract

Air pollution is the most severe environmental problem in the world in terms of human health. The World Health Organisation (WHO) estimates that 91% of the world's population is exposed to high air pollutant levels. The risks are particularly high in urban areas, where often high population densities are combined with high air pollutant levels. Urban street canyons are especially prone to high pollutant levels due to the proximity of traffic and reduced exchange of air with the street canyon and air above, referred to as ventilation. As a result, one of the most important topics in city planning is how to avoid designs that impact the air quality negatively.

Street trees are often planted in street canyons for aesthetic purposes while they can also improve thermal comfort. The air quality within street canyons is affected by street trees in two ways. They provide leaf surface for air pollutants to deposit on, thus cleaning the air. On the other hand, they block the airflow within the street canyon, thus decreasing the ventilation of air pollutants. In previous studies the latter effect has generally been found stronger. However, due to the various benefits of street trees, leaving them completely out from street canyon designs is rarely an option.

The City of Helsinki is planning to develop its current inbound motorways into city boulevards which has raised concerns towards the local air quality levels due to high projected traffic rates. The aim of this study was to find which of five street-tree scenarios, realistic for the city boulevards, is the best in terms of air quality. Pedestrian-level aerosol mass concentrations were used as the measure of air quality. Furthermore the impacts of vegetation and dependency of aerosol mass concentrations on various flow statistics were studied in order to explain the differences between the scenarios. Large-eddy simulation (LES) model PALM was utilised to study the flow field above and within a city boulevard and to model the dispersion of traffic-related aerosols. Aerosol particles of different sizes were represented using a sectional aerosol model SALSA. The suitability of the used LES setup for such intercomparison studies was also investigated.

The results showed that the street trees have generally a considerable negative impact (-2% to 54%) on pedestrian-level aerosol mass concentrations. Trees were find to reduce the mean wind speeds within the street canyon, which correlated strongly with the pedestrian-level concentrations. This was particular with a parallel wind direction to the street canyon due to decreased ventilation. Turbulence produced by the street trees was partially able to compensate for the reduced ventilation in some scenarios. The increased turbulence could be observed up to heights exceeding the maximum building height.

Based on the results, it is recommended to prefer variable-height street-tree canopies over uniform ones within street canyons similar to the studied one. Uneven canopy increases turbulence and related pollutant transport which partially compensates decreased ventilation due to decreased wind speeds. It is also recommendable to consider minimising the ratio of the total crown volume to the street canyon volume, as ventilation decreases sharply as the ratio increases.

Avainsanat — Nyckelord — Keywords
CFD, LES, turbulence, air pollution, street canyon, pollutant dispersion, urban vegetation, ventilation

Säilytyspaikka — Förvaringsställe — Where deposited
HELDA - Digital Repository of the University of Helsinki

Muita tietoja — övriga uppgifter — Additional information

HELSINGIN YLIOPISTO — HELSINGFORS UNIVERSITET — UNIVERSITY OF HELSINKI

Tiedekunta — Fakultet — Faculty	Koulutusohjelma — Utbildningsprogram — Education programme
Matemaattis-luonnontieteellinen tiedekunta	Ilmakehätieteiden maisteriohjelma

Tekijä — Författare — Author
Sasu Karttunen

Työn nimi — Arbetets titel — Title
The effect of vegetation configuration on the pedestrian-level aerosol mass concentrations in a wide street canyon

Pääaine — Huvudämne — Major
Meteorologia

Työn laji — Arbetets art — Level	Aika — Datum — Date	Sivumäärä — Sidoantal — Number of pages
Pro gradu	16.05.2020	59 sivua

Tiivistelmä — Referat — Abstract

Ilmansaasteet ovat ihmisten terveyden kannalta maailman vakavin yksittäinen ympäristöongelma. Maailman terveysjärjestö WHO:n arvion mukaan 91% maailman väestöstä altistuu toistuvasti korkeille ilmansaastepitoisuuksille. Haittavaikutukset ovat erityisen suuria kaupunkialueilla, joissa korkea asukastiheys yhdistyy korkeisiin ilmansaastepitoisuuksiin. Katukuilut ovat erityisen ongelmallisia ilmanlaadun kannalta, sillä liikenteen päästöjen tuulettuminen pois katukuilusta on heikompaa kuin avoimilla alueilla. Tästä johtuen katukuilujen ilmanlaatu pyritään ottamaan usein huomioon jo kaupunkisuunnittelussa.

Leveisiin katukuiluihin istutetaan usein puita esteettisistä syistä, mutta niillä on positiivinen vaikutus myös lämpömukavuuteen. Katupuut vaikuttavat katukuilujen ilmanlaatuun kahdella eri tavalla. Ilmansaasteiden tarttuminen niiden lehtiin, oksiin ja runkoon vähentää niiden pitoisuutta ilmassa, mutta toisaalta puiden tuoma ilmanvastus heikentää ilmansaasteiden tuulettumista pois katukuilusta. Aiemmissa tutkimuksissa tuulettumisen heikkenemisen on havaittu olevan näistä merkittävämpi tekijä. Koska katupuilla on kuitenkin myös positiivisia vaikutuksia kaupunkiympäristöjen viihtyisyyteen, joten niiden jättäminen kokonaan pois on harvoin vaihtoehto.

Helsingin kaupungin vuonna tuoreimman yleiskaavan mukaan nykyiset kaupunkiin johtavat moottoritiet Tuusulanväylä ja Vihdintie muutetaan kaupunkibulevardeiksi. Tämän tutkimuksen tavoitteena oli selvittää, mikä viidestä eri kaupunkibulevardeille soveltuvasta katupuuvaihtoehdoista olisi ilmanlaadullisesti paras. Ilmanlaadun mittarina käytettiin aerosolien massapitoisuuksia katutasolla. Lisäksi tutkimuksessa tarkasteltiin puiden vaikutusta ilman virtausta kuvaaviin tilastollisiin suureisiin ja tutkittiin katutason hiukkaspitoisuuksien riippuvuutta näistä. Tutkimuksessa käytettiin LES-mallia PALM tuottamaan tarkka kuvaus ilman virtauksesta kaupunkibulevardilla ja sen yläpuolella. Eri kokoisten hiukkasten kulkeutumista virtauksen mukana sekä niiden tarttumista kasvillisuuteen ja pinnoille tarkasteltiin aerosolimallilla SALSA. Lisäksi tutkittiin käytetyn LES-malliasetelman soveltuvuutta vastaaviin vertailututkimuksiin.

Tulokset osoittavat että katupuilla on pääsääntöisesti selvä negatiivinen vaikutus (-2% – 54%) katutason ilmanlaatuun. Ne vähentävät merkittävästi tuulen keskinopeutta katukuilussa, jonka havaittiin olevan vahvasti kytköksissä katutason pitoisuuksiin ja tuulettumisen heikkenemiseen etenkin katukuilun suuntaisilla tuulilla. Katupuiden virtaukseen tuottama turbulenssi pystyi kompensoimaan tätä vaikutusta osittain joissain kasvillisuusvaihtoehdoissa. Voimistunut turbulenssi oli havaittavissa aina kattokorkeuden yläpuolelle asti.

Tulosten perusteella vastaavien katukuilujen kasvillisuudessa tulisi suosia vaihtelevakorkuisia katupuulatvustoja yhtenäisten latvustorakenteiden sijaan. Epätasaisen latvuston tuottama turbulenssi kompensoi osaltaan alentuneiden tuulennopeuksien aiheuttamaa heikentynyttä tuulettumista. Puun latvuston kokonaistilavuutta suhteessa katukuilun tilavuuteen tulisi myös tarkkaan harkita, sillä tällä on positiivinen yhteys tuulettumisen heikkenemiseen.

Avainsanat — Nyckelord — Keywords
CFD, LES, turbulenssi, ilmanlaatu, ilmansaasteiden leviäminen, katukasvillisuus, tuulettuminen

Säilytyspaikka — Förvaringsställe — Where deposited
HELDA – Helsingin yliopiston digitaalinen arkisto

Muita tietoja — övriga uppgifter — Additional information

Contents

1 Introduction

Air pollution is a major worldwide environmental problem, with many detrimental health implications for humans and animals (Manisalidis et al., 2020). According to the estimates by World Health Organisation (WHO), air pollution is a cause for approximately seven million deaths every year, with 91% of the world's population exposed to air containing high levels of air pollutants (World Health Assembly, 2015). In Finland, a country with a comparably good air quality air pollution is attributable to 1600-2000 premature deaths yearly (Ministry of the Environment, 2019). Due to the health risks as well as subsequent economic and societal impacts, air pollutant emissions and concentrations are regulated in many regions, including the European Union (EU) (EEA, 2019).

Street canyons are especially prone to high air pollutant concentrations due to the lower wind speeds combined with street-level emissions from traffic. This makes street canyons susceptible for exceedances of the threshold values in air quality regulations, posing a health risk for the pedestrians, cyclists and residents that are exposed to the poor air quality on a daily basis. Thus optimising street canyons for the best air pollutant removal performance by maximising their ventilation is in the interests of city planners around the world (Yazid et al., 2014). Vegetation is often brought up as a possible air pollution mitigation method (Vos et al., 2013). Whilst tree leaves are capable of trapping various air pollutants, multiple studies have concluded that the net effect of street trees on air quality within a street canyon is generally negative due to the decreased ventilation of air pollutants from the street level (Abhijith et al., 2017). Although their negative impact on air quality, street trees are important for urban environments, for example in terms of aesthetics (Locke et al., 2015) and improve thermal comfort (Coutts et al., 2016).

Only a limited number of field studies have been carried out on the effect of street trees on air quality within street canyons (Abhijith et al., 2017). The vegetation configuration cannot be altered in great extent in real street canyons and the studies are thus limited to compare similar street canyons with different vegetation configurations (Kikuchi et al., 2007; Salmond et al., 2013; Jin et al., 2014). This can result in inaccuracies, as the observed differences in pollutant concentrations might be influenced by other environmental factors, such as surrounding urban form, which are not necessarily the same for all street canyons (Kikuchi et al., 2007). Partially for these reasons, the previous studies on the matter have been generally done using either wind tunnel laboratory experiments or numerical simulations (Abhijith et al., 2017). However, representing emission sources and air pollutant processes in wind tunnels is difficult (Oke et al., 2017). The majority of the previous numerical simulations have been performed using Reynold-averaged Navier-Stokes

simulations (RANS), which has found to lack in accuracy for complex urban environments (Tominaga and Stathopoulos, 2010, 2011). Therefore more accurate simulations with a more comprehensive description of air pollutants within the simulations are needed to better understand the effect of vegetation on air quality within street canyons. Today, large-eddy simulation (LES) is generally considered as a promising alternative, providing a great advantage in terms of accuracy compared to RANS (O'Neill et al., 2016).

In Helsinki, Finland, air quality has gained increased attention from the urban planning perspective in recent years although the situation has been at a relatively good level compared to other European capitals (HSY, 2016). The latest air quality plan from 2017 states that various measures, including taking air quality into account already in the planning phase of new neighbourhoods or districts, should be applied to mitigate the air quality issues in Helsinki. The latest Helsinki city plan which came into effect in December 2018 introduced an urban development concept of city boulevards (City of Helsinki, 2016). A city boulevard is a wide heavy-traffic street canyon surrounded by mid-rise buildings. These city boulevards are intended to replace the current motorways leading into downtown Helsinki, with an intention of increasing the land area available for city densification. Additionally, a city boulevard is meant to be a comfortable space for residents and bypassers as well as a trunk route for public and private transport. The street area of a city boulevard is intended to be shared by pedestrians, motor vehicles, trams and cyclists. As the existing motorways are traffic-heavy, the traffic rates on the city boulevards are also projected to be high. This poses a potential health risk for the residents and bypassers due to the vicinity of the traffic air pollutant source.

In this study, different vegetation scenarios that could be realistically used at the city boulevards are compared with an aim to understand which of the scenarios is the best in terms of their air pollutant removal performance. The air pollutant removal performance of the scenarios is studied using pedestrian-level aerosol mass concentrations. Furthermore, the dependency of the pedestrian-level aerosol mass concentrations on mean wind and turbulence statistics is studied. The study utilises LES technique to resolve the flow in different scenarios, with simulated conditions corresponding a dry late spring morning. A sectional aerosol model is used conjointly with the LES model to represent the dispersion and dry deposition of aerosol particles. The simulation setup, utilising LES-LES self-nesting and turbulence recycling methods, is used to produce similar quasi-stationary flow conditions for all the scenarios. Additionally, suitability of the simulation setup for similar intercomparison dispersion studies is investigated.

2 Theory and background

2.1 Turbulent flows

2.1.1 Characteristics

Turbulent flows are characterised by chaotic 3-dimensional variations, eddies, in the flow variables, namely flow velocity and the pressure field. Compared to laminar flows, fluid properties are effectively mixed in turbulent flows due to turbulent eddies. The flow is turbulent when the inertial forces in the flow dominate the viscous forces. The ratio of inertial forces and viscous forces is described by the Reynolds number

$$\mathrm{Re} = \frac{Ul}{\nu}, \tag{2.1}$$

where U is the characteristic velocity, l is the characteristic length scale and ν is the viscosity of the fluid. Flows where the Reynolds number exceed $\mathrm{Re} = 6000$ are generally considered turbulent, although the transition from laminar to turbulent flow happens through a range of Reynolds numbers (Pope, 2000). The turbulent flows are subsequently sometimes called high Reynolds number flows.

2.1.2 Navier-Stokes equations for incompressible fluids

Conservation of mass for a fluid is described by the continuity equation

$$\frac{\partial \rho}{\partial t} + \nabla \cdot (\rho \mathbf{u}) = 0, \tag{2.2}$$

where $\frac{\partial \rho}{\partial t}$ is the local time derivative of density ρ and $\mathbf{u}(x, y, z, t)$ is the flow velocity. Assuming an incompressible fluid ($\rho = \rho_0$), we can write the continuity equation as

$$\nabla \cdot \mathbf{u} = 0. \tag{2.3}$$

The assumption of fluid incompressibility implies that the there is no compression or expansion of the fluid, thus effectively stating no variations in the fluid density occur (Holton, 2004; Stull, 1988).

The corresponding equation for conservation of momentum is

$$\frac{\partial \mathbf{u}}{\partial t} + (\mathbf{u} \cdot \nabla)\mathbf{u} = \mathbf{g} - 2\boldsymbol{\Omega} \times \mathbf{u} - \frac{1}{\rho_0}\nabla p + \nu \nabla^2 \mathbf{u}, \tag{2.4}$$

where ν is the kinematic viscosity of the fluid, ρ_0 is the constant density, $-2\boldsymbol{\Omega} \times \mathbf{u}$ is the acceleration caused by rotation of the Earth i.e. Coriolis force, $\mathbf{g}$ is the effective gravity

combining both the gravitational acceleration and the centrifugal inertial force. This form ignores the effect of spherical metrics of the Earth which is negligible in the planetary boundary layer (Holton, 2004). Together the Eqs. (2.3) and (2.4) form the Navier-Stokes equations for incompressible fluids in rotating coordinate frame.

Using Einstein's summation notation, a Cartesian vector $\mathbf{x}$ can written using implicit summation as

$$\mathbf{x} = \begin{bmatrix} x_1 \\ x_2 \\ \vdots \\ x_n \end{bmatrix} = \sum_{i=1}^{n} x_i \mathbf{e}_i = x_i \mathbf{e}_i, \tag{2.5}$$

where $\mathbf{e_i}$ is the Cartesian orthonormal unit vector of dimension i (Pope, 2000). Using the summation notation the Navier-Stokes equations for incompressible flow can be written as (following Stull, 1988 and Pope, 2000)

$$\nabla \cdot u_i = 0 \tag{2.6}$$

and

$$\underbrace{\frac{\partial u_i}{\partial t}}_{\text{I}} + \underbrace{u_j \frac{\partial u_i}{\partial x_j}}_{\text{II}} = \underbrace{-\delta_{i3} g}_{\text{III}} \underbrace{- 2\epsilon_{ijk}\Omega_j u_k}_{\text{IV}} \underbrace{- \frac{1}{\rho_0}\frac{\partial p}{\partial x_i}}_{\text{V}} + \underbrace{\nu \frac{\partial^2 u_i}{\partial x_j^2}}_{\text{VI}}, \tag{2.7}$$

where δ_{ij} is the Kronecker delta defined as

$$\delta_{ij} = \begin{cases} 1, & \text{if } i = j \\ 0, & \text{if } i \neq j \end{cases} \tag{2.8}$$

and ϵ_{ijk} is the Levi-Civita symbol defined as

$$\epsilon_{ijk} = \begin{cases} 1, & \text{if } (i,j,k) \text{ is } (1,2,3),\ (2,3,1) \text{ or } (3,1,2) \\ -1, & \text{if } (i,j,k) \text{ is } (3,2,1),\ (1,3,2) \text{ or } (2,1,3) \\ 0, & \text{if } i = j,\ j = k \text{ or } k = i. \end{cases} \tag{2.9}$$

The descriptions of the terms in equation Eq. (2.7) are summarised in Table 2.1.

A strict assumption of constant density used in Eq. (2.7) cannot be used for most meteorological purposes as in atmospheric phenomena density variations have significant effect to the flow dynamics. A common way to approach the problem is the Boussinesq-approximation, which handles the density variations and subsequent buoyancy as a linear function of temperature T in the gravitational terms ignoring them elsewhere. This approach is suitable for situations where the vertical length scales are much smaller than the horizontal, i.e., no deep convection is present (Tritton, 1988). Practical application of the approximation for dry air is to replace the effective gravitational acceleration g

Table 2.1: The descriptions of the terms in equation Eq. (2.7) based on Stull (1988).

Term	Description
I	Storage of momentum as the local fluid velocity.
II	Advection of momentum.
III	Effective gravitational acceleration, the sum of the true gravitational acceleration and the centrifugal force.
IV	Coriolis force, an inertial force caused by the rotating frame of reference.
V	Pressure gradient force caused by the inhomogeneity of the pressure field.
VI	Viscous force caused by molecular viscosity.

with $\left[g\left(\frac{T-\langle T\rangle}{\langle T\rangle}\right)\right]$ (where $\langle ...\rangle$ denotes a spatial average) in Eq. (2.7) (Garratt, 1992). For convenience potential temperature defined as

$$\theta = T\left(\frac{p_0}{p}\right)^{R/c_p}, \tag{2.10}$$

where c_p being the specific heat of dry air, is commonly used instead of temperature (Tritton, 1988). Subsequently the Bousinnesq-approximated non-hydrostatic equation for conservation of momentum in dry air can be written as

$$\frac{\partial u_i}{\partial t} + u_j\frac{\partial u_i}{\partial x_j} = -\delta_{i3}g\left(\frac{\theta - \langle\theta\rangle}{\langle\theta\rangle}\right) - 2\epsilon_{ijk}\Omega_j U_k - \frac{1}{\rho_0}\frac{\partial p}{\partial x_i} + \nu\frac{\partial^2 u_i}{\partial x_j^2}. \tag{2.11}$$

For synoptic and global scales hydrostatic version, which use hydrostatic approximation in place of the vertical component in the momentum equation, can be used as this simplifies possible computations. However, successful modelling of mesoscale or local scale phenomena generally requires the non-hydrostatic equations (Wedi et al., 2009).

2.1.3 Statistical description of turbulence

Any time-dependent quantity $A(t)$ of the flow can be decomposed to a temporal mean $\overline{A}$ and a time-dependent deviation from the temporal mean $A'(t)$ using Reynolds decomposition as

$$A(t) = \overline{A} + A'(t). \tag{2.12}$$

By applying Reynolds decomposition to the flow field itself, one can write the kinetic energy of a turbulent flow E_k as a sum of mean kinetic energy K and turbulent kinetic energy k

$$E_k = \frac{1}{2}u_i^2 = K + k, \tag{2.13}$$

where

$$K = \frac{1}{2}\overline{u_i}^2 \tag{2.14}$$

and

$$k = \frac{1}{2}\overline{u_i'^2}. \tag{2.15}$$

As for the equations of motion, both energies are expressed here per unit mass.

The production and dissipation of k is described by turbulent kinetic energy equation

$$\frac{\partial k}{\partial t} + \overline{u_i}\frac{\partial k}{\partial x_i} = MP + BPL + TR - \epsilon, \tag{2.16}$$

where MP is the mechanical production, BPL is the buoyant production or loss, TR is redistribution by turbulent transport and pressure forces and ϵ is the dissipation (Holton, 2004). The mechanical production of k is caused by wind shear in the mean flow. Its greatest source is the shear induced by the surface roughness elements. The magnitude of the mechanical production depends on the surface geometry as well as on the ambient wind speed. As for the flow in general, the buoyancy is able to either accelerate or damp the vertical motions in turbulence. In unstable condition,s the turbulence is generated by this acceleration and in stable conditions it is consumed by the buoyancy damping. In addition to advection with mean flow, turbulence can be transported by itself. This and the redistribution of the turbulence by pressure perturbations are combined in term TR. Finally, turbulence is dissipated into heat at small scales by viscous forces. This is taken into account by the inclusion of the dissipative term ϵ, which is always a sink of turbulence kinetic energy (Stull, 1988).

In turbulent flows, quantities such as mass, heat, air pollutants and momentum are transported by the fluid motion (Stull, 1988). This transportation is quantified as fluxes, representing transport of a quantity per unit area per unit time. Part of the transport is described by advective fluxes caused by the mean flow and the rest by turbulent fluxes caused by turbulent motions. In atmosphere, the advective fluxes are generally larger, but turbulent fluxes are important near the surface especially in the vertical direction. The advective fluxes can be represented using temporal mean variables as

$$F_{a,i,\text{advective}} = \overline{u_i}\,\overline{a}, \tag{2.17}$$

where a is the transported quantity. Turbulent fluxes are described by temporal mean covariance of transported variable and flow field as

$$F_{a,i,\text{turbulent}} = \overline{u_i' a'}. \tag{2.18}$$

These forms of both advective and temporal fluxes are called kinematic fluxes. While they don't directly give the rate of transport of given quantity, they are usually straightforward to compute directly from observations. To present the actual rate of transport of given quantity, one must convert the kinematic flux to dynamic flux. For example the dynamic flux of momentum is its kinematic flux multiplied by the fluid density ρ:

$$\widetilde{F}_{u,i,\text{advective}} = \rho\overline{u_i}\,\overline{u_j}, \tag{2.19}$$

$$\widetilde{F}_{u,i,\text{turbulent}} = \rho\overline{u_i' u_j'}. \tag{2.20}$$

The latter flux, the turbulent momentum flux, is a second order tensor, usually referred as the Reynolds stress. Usually in meteorology the most interesting turbulent fluxes are the vertical ones. Vertical momentum flux is

$$F_{u,k,\text{turbulent}} = \sqrt{\overline{u_i' u_k'}^2 + \overline{u_j' u_k'}^2}, \tag{2.21}$$

where u_i and u_j are the horizontal wind velocity components and u_k is the vertical wind velocity.

2.2 Atmospheric boundary layer

2.2.1 Characteristics, formation and structure

Troposphere, the lowest layer of Earth's atmosphere where most of the weather phenomena take place, can be further divided into two layers with distinctive dynamical properties. In the lower layer, the atmospheric boundary layer (ABL), the atmospheric flow is disturbed due to the interaction caused by the Earth's surface causing the flow to be highly turbulent in nature. In the layer above it, the free atmosphere, the direct effects of the surface are negligible.

The turbulence in the ABL is produced either mechanically or thermally as described in the section Section 2.1.3. The characteristics and magnitude of the production and the dissipation of turbulence in the ABL depends on the surface properties as well as on meteorological conditions. However, the ABL doesn't react instantaneously to changes in surface properties. It takes time for turbulent fluxes to transport the effects of the changed surface forcing up the ABL. Therefore a new, internal boundary layer (IBL), is formed downwind to the location where surface properties change. An IBL extends vertically going further downwind, ultimately replacing the original BL, given that the surface properties don't change downwind. After new IBL has completely replaced the original BL, the ABL is said to be fully developed. In fully developed BL, the flow is quasi-stationary, effectively stating that the mean flow properties are constant in time (Tennekes and Lumley, 1972).

The ABL can be further subdivided into five sublayers from down to up based on their dynamic characteristics: the viscous sublayer, the roughness sublayer, the inertial sublayer, the mixed layer and the entrainment zone (Stull, 1988).

The viscous sublayer, the layer nearest to a surface such as ground, building wall or tree leaf, is the only layer in the ABL where the viscous stress is much higher than the Reynolds stress resulting in laminar flow (Pope, 2000). As the viscosity of air is very low

($\nu \sim 10^{-5}$ Pa s), the viscous sublayer in the ABL is very thin, only an order of millimetres thick (Holton, 2004).

The roughness sublayer is a highly turbulent layer above the viscous sublayer. The mean flow statistics in the roughness sublayer are spatially non-uniform due to the effect of the vicinity of roughness elements, ranging from the size of a pebble to high-rise apartment buildings. In the roughness sublayer the turbulent length scales are similar to the roughness element height, thus the flow is locally highly influenced by them (Raupach et al., 1991). Part of the roughness sublayer exists within the canopy (buildings, trees, etc.) itself, this part of the roughness sublayer is often referred to as the canopy layer (Shaw et al., 1983). Laboratory studies (O'Loughlin and Annambhotla, 1969; Mulhearn, 1978; Raupach et al., 1980, 1986) have shown that the roughness layer height is between two to five times the height of individual roughness elements.

The inertial sublayer exists above the roughness sublayer. The main dynamical property of it is the approximately vertically constant fluxes (momentum, heat and scalars) throughout the layer. As the inertial sublayer is more spatially uniform than the roughness layer, the spatial representativeness of a flux at individual point is generally larger than in the roughness layer. Another consequence, although an indirect one, is that due to the nearly constant momentum flux, the wind profile in the layer follows an approximately logarithmic profile, decreasing downwards. This is in contrast with the roughness sublayer, where the wind profile is found to follow the logarithmic profile only when extensive spatial averages are considered. In some urban environments where the underlying roughness constantly changes, the inertial sublayer might not exist at all (Cheng and Castro, 2002). The roughness and the inertial sublayers which are together referred to as the surface layer. Above the surface layer, the structure of the ABL depends heavily on stability and synoptic-scale phenomena (Stull, 1988). This study however focuses primarily on the phenomena within the surface layer as this is the most important layer for local scale air quality variations.

2.3 Urban boundary layer

Above the urban areas, an IBL called the urban boundary layer (UBL) is formed. The surface properties in urban areas are heavily modified by human influence, the ABL above urban areas differ much from natural such as rural and oceanic boundary layers. The roughness sublayer is typically very thick and the mechanical production of turbulence is strong in urban areas due to the size of the prominent roughness elements: buildings. The impermeable nature of urban surfaces and smaller incidence of vegetation compared to typical rural areas causes decreased evapotranspiration and increased surface temperatures. In addition, waste heat from anthropogenic sources increases the temperatures of built surfaces. These factors increase the sensible heat flux, i.e. the transfer of thermal

energy that can be measured in terms of temperature, from surface to atmosphere. As a consequence that the UBL is rarely stable and thermal turbulence generation is generally stronger than in rural areas. Urban surface properties are diverse and various combinations of different surface properties exist. Various classifications have been formulated to describe different urban surfaces at general level, including Local Climate Zone classification by Stewart and Oke (2012). However, local scale studies require more detailed description of urban surface properties.

The imminent effect of urban topography, including both natural land shape and built structures, for the UBL is the increased surface friction it causes for the airflow. An urban surface is aerodynamically rough, with roughness length, a length scale describing the roughness elements of a surface, varying between 1 and 7 metres, compared to 0.7 to 3 metres for forests and 0.0001 to 0.002 for water surfaces (Hansen, 1993). As the aerodynamic roughness cannot be directly calculated from the surface topography, several other metrics for description of the surface shape and morphometry are used. The most commonly used measures to describe urban roughness are the average building height $H_{b,avg}$, the building height standard deviation $H_{b,std}$ and the dimensionless ratios plan area fraction λ_p (i.e., the fraction of area occupied by buildings) and frontal area fraction λ_f (i.e., the fraction of the frontal area of buildings to the total plan area) (Macdonald et al., 1998).

2.3.1 Flow within the urban canopy layer

The flow between the buildings, namely within the urban canopy layer, is highly turbulent due to the complex geometries and constant interaction with the flow above the canopy layer. The surrounding buildings provide a shelter for the air within the street canyon, thus separating it from the air above with a shear layer located approximately at roof height. The separation of the flow between the urban canopy layer and flow above makes various flow patterns possible to emerge. One of the most studied of these is a canyon vortex which can form in a street canyon when the mean wind is parallel to it (Letzel et al., 2008). The canyon vortex is essentially a recirculation pattern within a street canyon while only a little air is exchanged from or to the vortex through the shear layer. The size and the anisotropy of the vortex depends on the street canyon morphology, with multiple stacked or parallel vortices possible for deep or wide street canyons (Letzel et al., 2008). The amount of sheltering provided by the buildings and the vortex formation has a strong dependency on the aspect ratio, i.e., the height-to-width ratio of the street canyon, this dependency is illustrated in Fig. 2.1 (Oke, 1988). For oblique wind directions, helical vortices are possible (Lietzke and Vogt, 2013). When wind direction approaches to being parallel to the street canyon, the shear layer disappears and the flow within the street canyon reattaches to the flow above, increasing wind speeds within the canyon (Kastner-Klein et al., 2001). The possible flow patterns within the canopy layer are easily altered and destroyed by gusts of

air penetrating the shear layer (Eliasson et al., 2006). As a consequence estimating street canyon ventilation, i.e. the exchange of air between the street canyon and the air above it is difficult to predict and depend on multiple mechanisms and factors which some remain poorly understood (Salizzoni et al., 2009; Yazid et al., 2014).

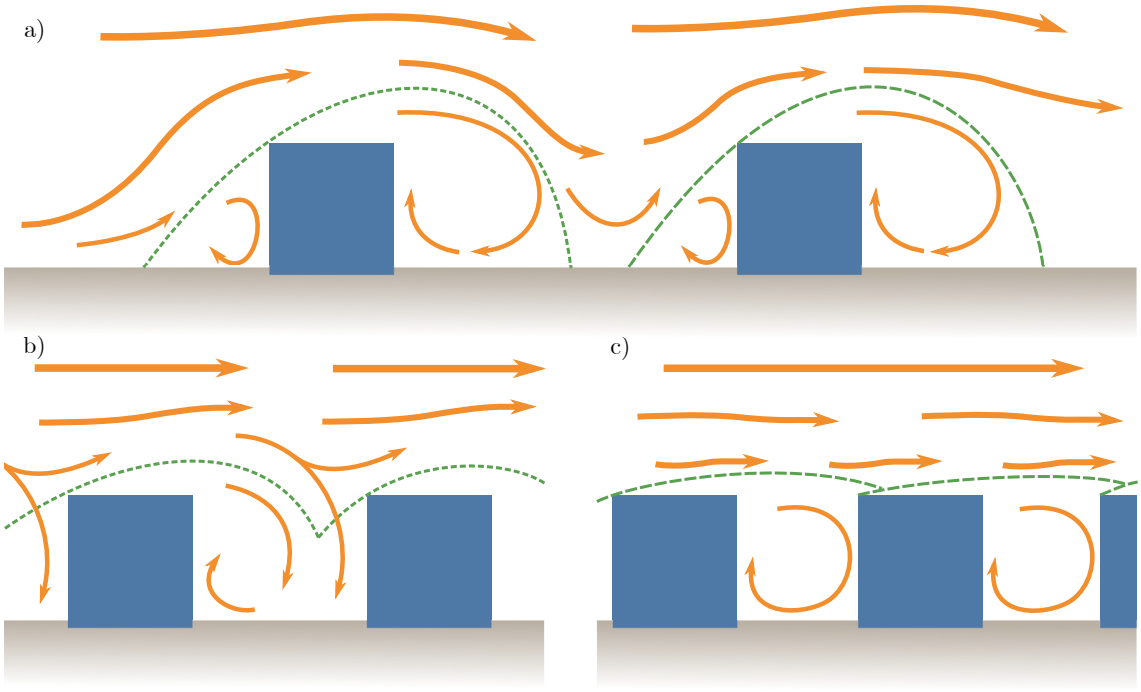

Figure 2.1: The effect of the aspect ratio of street canyons on sheltering and the formation and the shape of the canyon vortex. For isolated roughness elements (a), the buildings provide only restricted sheltering, allowing the wind to enter the street canyon aloft. In wake interference flow (b), the buildings provide more sheltering, allowing wind to enter the street canon only occasionally. High aspect ratios can result in skimming flow (c), where the canyon vortex has only limited interaction with the flow above. The figure is adapted from Oke (1988).

Although urban form is much dominated by built environment, vegetation affects the airflow and energy transport also in urban areas. Regionally much of these effects scale with simple parameters such as the plan area fraction of the vegetation λ_v, but locally, for example within street canyons and parks, the effects are much more complex and depend on plant architecture and physiology (Raupach et al., 1996; Dupont and Brunet, 2009; Oke et al., 2017). However, it is important to note that these two are not independent from each other, with the factors of plant architecture such as foliage density and canopy form depending partially on plant physiology, for example on plant species, age and health.

The immediate effects of the vegetation on airflow are the form and viscous drag forces caused by canopy foliage, branches and trunks. Thus vegetation acts a sink of momentum and subsequently turbulence kinetic energy of the flow (Thom, 1972; Poggi et al., 2004). The standard way of taking this into account in the governing equations is introducing an

additional sink term f_v of form

$$f_v = -C_{Dv} \text{ LAD } \sqrt{u_i^2} u_i, \tag{2.22}$$

into the momentum equation. Here C_{Dv} is the canopy drag coefficient, LAD is the one-sided leaf area density, a common measure of foliage density (Eq. (2.11); Katul et al., 2004).

Canopy form and foliage density are the most important factors for these drag forces although biomechanics also have an influence through leaf reconfiguration (Albayrak et al., 2014; Vogel, 1989). Unlike drag caused by built environment, plant canopy drag can be seasonal in nature. For instance, deciduous plants drop their leaves in wintertime which in turn reduces the foliage density and thus the drag induced to airflow substantially (Giometto et al., 2017).

Vegetation also modifies heat and moisture fluxes between the atmosphere and urban surfaces. These fluxes cause secondary effects to airflow, as they alter the stability of the boundary layer. Nevertheless, even in strictly neutral flows the successful description of the local effects of vegetation on airflow requires knowledge of foliage density and canopy form. Additionally, some knowledge on plant biomechanics is required, as it affects the C_{Dv} and thus the relation between LAD, wind speed and the drag forces.

2.3.2 Air pollutants

Air pollutants can be divided into two categories: gas molecules and aerosols suspended in the air. An aerosol is a general term referring to any solid or liquid particles suspended in a gas, thus not limited only to air pollutants (Hinds, 1999). The air pollutant concentrations within the atmosphere vary greatly by location and height, with areas of high anthropogenic sources of air pollutants having the highest concentrations. The vast majority of the air pollution originate from human activities, such as the combustion of fossil fuels (EEA, 2019). Thus the heavily polluted air is typically found in heavily industrialised areas where coal or lignite is used to produce energy. However, air pollutant concentrations tend to be high also in unindustrialised urban areas due to high traffic rates and use of combustion-driven motor vehicles (Hussein et al., 2004).

Unlike gaseous air pollutants, aerosols undergo gravitational settling affecting their dynamic behaviour. Consequently they are not advected in the upward direction as easily as gas molecules, making it harder for them to escape cavities such as street canyons (Oke et al., 2017). As the aerosol processes and dynamic behaviour can be highly dependent on the particle size, size-specific modelling is required for detailed local scale representation. The behaviour of aerosol particles within a street canyon depends on their size and shape, thus representing them as passive scalars within the flow might not result in accurate descriptions (Hinds, 1999).

The aerosol concentrations are usually given as a mass concentration. Two commonly

used metrics are the mass concentration of sub-2.5 µm ($PM_{2.5}$, PM being short for particulate matter) and sub-10 µm (PM_{10}) particles. Although not commonly included in monitoring measurements, $PM_{0.1}$ can be used for sub-100 nm ultrafine particles. The health effects of ultrafine particles are less studied than those for PM_{10} and $PM_{2.5}$, but some evidence suggest that they might make a significant contribution to the overall toxicity of aerosols, mainly due to their capability to enter the cardiovascular system from the respiratory system (Terzano et al., 2010). WHO has set guidelines for PM_{10} and $PM_{2.5}$ mass concentrations for protection of health (WHO, 2006). Additionally, the EU enforces threshold values after which local and governmental authorities are obligated to develop and implement measures to mitigate the concentrations (European Union, 2008). Both WHO guidelines and the EU limits are summarised in Table 2.2. No guideline or threshold values for $PM_{0.1}$ by the WHO or the EU currently exist.

Table 2.2: A summary of WHO guidelines and threshold values set by the EU for PM_{10} and $PM_{2.5}$ mass concentrations (WHO, 2006; European Union, 2008).

Pollutant	Averaging period	EU limit	WHO guideline
$PM_{2.5}$	Annual	25 µg m^{-3}	10 µg m^{-3}
	24-hour	-	25 µg m^{-3}
PM_{10}	Annual	40 µg m^{-3}	20 µg m^{-3}
	24-hour	-	50 µg m^{-3}
	Hourly	50 µg m^{-3} [i]	-

[i] Should not exceed on more than 35 days a year.

2.3.3 Aerosol particles in street canyons

Although the removal of aerosol particles from a street canyon depends strongly on the ventilation of air, it is also affected by dry deposition and gravitational settling, which are both size-dependent processes (Yazid et al., 2014; Abhijith et al., 2017). Thus the accurate description of aerosol particle ventilation from a street canyon requires a model that is both capable of accurately representing the complex flow field within the street canyon and is simultaneously capable of modelling the important, size-specific aerosol processes and dynamics. To estimate air pollutant removal and ventilation from the pedestrian-level in dry conditions, dry deposition on built surfaces, ground and vegetation has to be taken into account, as this can be a major sink of aerosol particles (Kurppa et al., 2019)

2.4 Computational fluid dynamics

As of this date, no smooth and globally defined solutions exist for the three-dimensional Navier-Stokes equations. Therefore, in practice, to predict the fluid velocity and pressure in space and time, one has to rely on either field or laboratory experiments or numerical simulation. Both approaches have their own advantages and disadvantages, hence leaving the task of balancing them for the research question in hand to the responsibility of the researcher. Experiments obey the laws of physics intrinsically and field experiments in particular have a naturally realistic setup. The major disadvantages in experimental methods are related to measurement and limited possibility to study multiple or future scenarios. A whole branch of numerical analysis, computational fluid dynamics (CFD), has emerged from the need to develop methods for numerical simulation of fluids.

2.4.1 Numerical approaches

The most common approaches in numerical methods begin with the discretisation of the problem. In this case the problem to be solved consists of the governing equations in a three-dimensional domain, a set of time- and space-dependent partial differential equations with their respective boundary conditions. The process of spatial discretisation has an objective of generating a three-dimensional smooth mesh (a model grid) out of geometric shapes (Blazek, 2005). Cartesian grids consisting of cuboids aligned with the Cartesian coordinates are the most common grids for atmospheric local- and mesoscale models as they provide relative simplicity for the data preparation and analysis (Blazek, 2005). After the grid generation, the continuous partial differential equations must be approximated in this grid. A few methods for this exist, with the finite difference method being popular in atmospheric science (Zikanov, 2010; Blazek, 2005). The finite difference method uses Taylor series to approximate the spatial partial derivatives over finite differences Δx_i with resulting truncation error depending on the degree of Taylor polynomial used and the grid spacing. After the spatial discretisation, the governing equations have to be discretised in time dimension for the prognostic variables. Multistage time-stepping schemes are commonly used due to numerical stability and efficiency they offer, with Runge-Kutta schemes being widely used (Chung, 2002).

As the Naiver-Stokes equations represent the flow of continuous fluid, an unique solution within a finite computational domain requires information on how to handle the model state variables at the computational domain boundaries. Selection of the boundary conditions is case specific and no universal formulation exists (Chung, 2002). Boundary conditions are usually mathematically formulated, but for example in some applications it is practical to obtain them from the state variables of a larger scale model. As simulation results depend heavily on these boundary conditions, special care has to be taken when formulating them (Blazek, 2005).

Finally, a model has to implement a method of solving the model equations at time-steps. There is a vast number of approaches also for this, with all having the common objective of approximating a model state which fulfils the governing equations with given boundary conditions (Chung, 2002).

2.4.2 Turbulence modelling

Since 1970's, due to increase in available computing power, it has been possible to directly model three-dimensional turbulent flows with numerical methods (Gatski et al., 1996). This approach, called the direct numerical simulation (DNS) is however impractical for much of the atmospheric use cases. As in DNS the whole spectrum of turbulence must be explicitly resolved, atmospheric studies are rarely interested in the smallest scales, DNS uses more computational resources than necessary (Gatski et al., 1996; Murphy, 2011).

For practical atmospheric applications, various turbulence models are used. The aim of using turbulence modelling in CFD is to decrease the amount of computational resources needed for simulations by reducing the amount of turbulence that is explicitly resolved in the simulation(Leschziner, 2015). A common approach is based on the Reynolds-averaged Navier-Stokes equations (RANS). By modelling the Reynolds stress tensor (Eq. (2.20)) in the RANS equations, it is possible to numerically approximate a time-averaged solution to the Navier-Stokes equations (Leschziner, 2015). The benefit of this approach is that the temporal evolution of the turbulent flow does not require explicit resolving, thus reducing the required computational resources compared to DNS. However, modelling of the Reynolds stress is a complex problem requiring the formulation of six additional relations for the unknowns in the tensor in order to close the RANS equations (Blazek, 2005; Gatski et al., 1996). Modelling these relations is not as accurate as explicitly resolving the turbulence and therefore RANS simulations lack in accuracy compared to DNS. Another major drawback of RANS simulations is that they provide only quasi-stationary solutions, i.e., solutions which are statistically constant in time.

A combination of direct numerical resolving of the Navier-Stokes equations for larger scales of turbulence and modelling the smaller scales is called the large-eddy simulation (LES). In LES the higher frequency fluctuations are separated from the lower frequencies by either spatial or spectral filtering process. The theory behind this scale separation is based on the observations that the smaller scale turbulence is more homogeneous than the larger eddies, thus making them easier to model. The modelled scale is referred to as the subgrid-scale (SGS) in LES terminology. Due to the homogeneous nature of this small scale turbulence, computationally lighter models can be used at the SGS to solve the Reynolds stress than those used in RANS. If the scale separation is done correctly, a majority of the kinetic energy and the fluxes of the flow are explicitly resolved (Blazek, 2005). The separation of turbulent scales in energy spectrum is illustrated in Fig. 2.2.

The consequence of resolving most of the turbulence explicitly is that LES generally

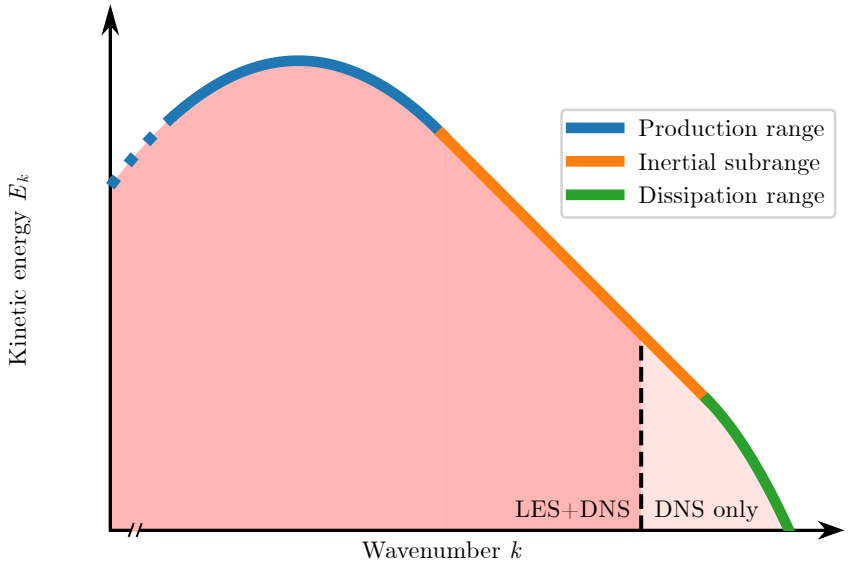

Figure 2.2: An illustrative diagram of a smoothed kinetic energy spectrum of a typical boundary layer flow. The resolved scales of LES and DNS are highlighted in light red, with the cutoff wavenumber between the resolved scales and the SGS of LES marked with a dashed line. Most of the energy spectrum is explicitly resolved in LES with a turbulence model used for the smaller scales. The whole energy spectrum is resolved explicitly in DNS.

outperforms RANS simulations in terms of accuracy, especially in complex cases including urban simulations. Accuracy and time-dependent solutions come with a price, though, with LES being orders of magnitude more expensive than RANS simulations (Walton and Cheng, 2002; Tominaga and Stathopoulos, 2010, 2011). Thus only since the beginning of the 1990's has LES emerged as a popular choice, due to significant growth in available computing resources (Blazek, 2005).

3 Methods

3.1 The PALM model system

The PALM model system is an LES implementation well-suited for urban applications (Maronga et al., 2020). It allows its core functionality to be extended using optional modules. In this study the plant canopy model and the sectional aerosol module SALSA are used in addition to the core LES model.

3.1.1 LES implementation

The PALM model system uses Boussinesq-approximated form of incompressible Navier-Stokes equations for atmosphere (PALM technical documentation, 2020). The equations for conservation of mass and momentum in continuous form are

$$\frac{\partial u_i}{\partial x_i} = 0, \tag{3.1}$$

and

$$\frac{\partial u_i}{\partial t} = -\frac{\partial u_i u_j}{\partial x_j} - \varepsilon_{ijk} f_j u_k + \varepsilon_{i3j} f_3 u_{g,j} - \frac{1}{\rho_0}\frac{\partial \pi^*}{\partial x_i} + g\frac{\theta_v - \langle\theta_v\rangle}{\langle\theta_v\rangle}\delta_{i3} - \frac{\partial}{\partial x_j}\left(\overline{u_i'' u_j''} - \frac{2}{3}e\delta_{ij}\right), \tag{3.2}$$

where subscript g denotes a geostrophic wind component and double primes ($''$) indicate SGS variables. π^* is the modified perturbation pressure defined as

$$\pi^* = p^* + \frac{2}{3}\rho_0 e, \tag{3.3}$$

where e is the SGS turbulent kinetic energy.

The PALM model system uses the finite difference method for spatial discretisation. The governing equations are averaged over Cartesian grid volumes in horizontally equidistant Arakawa C-grid. Arakawa C-grid is a staggered Cartesian grid where flow velocity components (u_i) are defined at cell edges and scalars at cell centres. This allows a direct computation of the finite spatial differences of the velocity components at cell centres and the derivatives of scalars at the cell edges, making it possible to approximate the spatial derivatives over only one grid length. This increases the effective resolution of the model by a factor of two compared to a non-staggered grid, but requires the interpolation of the flow velocity components before the flow vector can be calculated for the analysis. The averaging procedure over the grid volumes implicitly filters the model equations, effectively separating the SGS from the resolved scales. The temporal discretisation in PALM

is by default achieved by third order Runge-Kutta time-stepping scheme with adaptive step size. Advection of momentum and scalars are by default computed using the 5th order upwind scheme suggested by Wicker and Skamarock (2002).

The SGS model in PALM is based on a 1.5-order closure of the NS equations, with approximations for SGS fluxes based on the gradient transport theory in where the transport of momentum and scalars is considered proportional to its local mean gradient with a constant of proportionality K. In 1.5-order closure, the constant of proportionality for momentum K_m is computed using a prognostic equation for the SGS turbulent kinetic energy e (Moeng and Wyngaard, 1988).

The PALM model supports complex topographies and building geometries through three-dimensional masking. A boolean mask will be constructed based on the input, with the model equations being solved only at non-masked grid cells. Topography surfaces are treated with no-slip boundary condition, with wall functions based on Monin-Obhukov similarity theory used at SGS. Generally for boundaries PALM provides a selection of different boundary conditions, such as Dirichlet (fixed value), Neumann (fixed flux), cyclic and dynamic boundary conditions. Periodic boundary conditions can be used for horizontal boundaries. For non-periodic inlet boundary condition, a turbulence recycling method can be used. In the method, turbulent fluctuations at a recycling plane located downstream of the inlet are recycled back to the inflow boundary.

PALM parallelises the simulations by dividing the model domain into an evenly spaced horizontal processor grid. Thus the computations are spread on the processors assigned to simulation according to the processor grid. Since version 6.0, PALM has supported self-nesting in model runs (Maronga et al., 2020). In practice this means that the model can be run in one or more nested sub-domains within the main computational domain. The nesting approach allows for reduced computational costs without decreasing the domain size by allowing simulating the full domain in a coarser grid and areas of interest in a finer grid. It also allows sub-modules to be used only in smaller, nested domains, potentially reducing the amount of computational resources needed even further. The nesting can be run either in a one-way or a two-way mode. The one-way mode is effectively using the larger domain as a boundary conditions for the nested one, whilst in the two-way mode the domains can interact with each other.

3.1.2 Plant canopy model

PALM has an embedded plant canopy model to take the effect of vegetation into account in the model equations (PALM technical documentation, 2020). The effect of form and viscous drag induced to flow by the vegetation canopy is included in the momentum equation (Eq. (3.2)) with an additional sink term corresponding to Eq. (2.22). The effect of vegetation is also taken into account with an extra sink term for SGS turbulent kinetic

energy e as suggested by Shaw and Schumann (1992):

$$f_{e,v} = -C_{D,v}\ \mathrm{LAD}\ \sqrt{u_i^2}e. \tag{3.4}$$

The one-sided leaf area density LAD is represented in the model with a three-dimensional array with a corresponding LAD value for each grid cell in the domain. This array can be given to the model directly or it can be computed parametrically at model initialisation using beta probability density distribution following Markkanen et al. (2003).

3.1.3 Sectional aerosol model

A sectional aerosol model SALSA by Kokkola et al. (2008) has been embedded in PALM as of version 6.0 (Kurppa et al., 2019). It provides a possibility to simulate various size-dependent aerosol processes within an LES simulation. In the model, the aerosol size distribution is divided into discrete bins, with aerosol number concentrations, chemical compositions and processes computed individually for each bin. SALSA includes processes of nucleation, condensation, dissolutional growth, coagulation and dry deposition. The dry deposition is modelled as a negative surface flux of aerosol concentration

$$F_{N_i} = v_{d,i} N_{i,t-\Delta t_{SALSA}}, \tag{3.5}$$

where v is the dry deposition velocity and $N_{i,t-\Delta t_{SALSA}}$ is the aerosol number concentration of bin i at previous SALSA time step. For vegetation, the flux is scaled with LAD, as this represents the total leaf area per unit volume on which deposition can occur.

Solving for aerosol processes and dynamics comes with its price, as enabling SALSA increases the computational time of a simulation drastically. This can be partially mitigated by enabling only the processes important for the research question and increasing the time step Δt_{SALSA} on which the aerosol processes are computed. Even with just dry deposition enabled SALSA can increase the computational time by hundreds of percents (Kurppa et al., 2019).

3.2 Model setup

3.2.1 Built environment

The planning scenario used in the study was based on an simplified design of a city boulevard similar to one intended to replace the current Tuusulanväylä motorway according to the Helsinki city plan (City of Helsinki, 2016). Three versions of a 800-m-long section of a boulevard including one to two blocks of surrounding buildings were first constructed based on the referential model of a city boulevard in the city development plan (personal communication with the City of Helsinki on Jul 2, 2018). The three versions are differentiated by the boulevard width, which are 50 m, 54 m and 58 m. The street area of the

simplified city boulevard model consists of eight traffic lanes, four cycling lanes, tram lines running in the centre and pedestrian pavements on both sides. A width of a single motor traffic lane is set to 3 m.

Generic cuboid-shaped suburban roughness elements were then tiled around the boulevard. This was done in order to give a realistic representation of the future surrounding environment of the city boulevard in terms of aerodynamic roughness. Four different roughness elements were used, with their dimensions and shapes determined so that the average and standard deviation of building height as well as plan area fraction would correspond to ones computed for Oulunkylä and Pakila suburbs which surround the current Tuusulanväylä motorway in Northern Helsinki. The raster maps of Helsinki 3D open access point cloud data were used in computations (Auvinen, 2019; City of Helsinki, 2017).

3.2.2 Vegetation

Six different vegetation scenarios were considered with five of them realistic options for city boulevards (personal communication with the City of Helsinki on Jun 13, 2018) and one being a reference scenario with no vegetation. The scenarios included two species of street trees: *Tilia* × *vulgaris* (common lime) and *Sorbus intermedia* (Swedish whitebeam). Both are deciduous species, with *Tilia* being the most common genus in street and park trees in Helsinki (Timonen and Kauppinen, 2008).

An airborne laser scanning (ALS) inventory of urban roadside trees in Helsinki by Tanhuanpää et al. (2014) was utilised for creating three-dimensional models of trees for the simulations. First, *Tilia* × *vulgaris* and *Sorbus intermedia* trees were selected, and then the remaining trees were filtered by height. Individual *Tilia* × *vulgaris* trees with height $14 \leq H_v \leq 16$ m and *Sorbus intermedia* trees with height $8 \leq H_v \leq 10$ m were selected. This filtration process yielded 819 and 87 matches for *Tilia* × *vulgaris* and *Sorbus intermedia* respectively. Then, dimensionless vertical profiles were computed individually for both species based on the mean pulse return height distribution of the filtered trees. Finally, horizontally symmetric three-dimensional shapes for the tree crowns were constructed so that their diameter and horizontally integrated profile follow closely the ones derived from the ALS inventory (see Fig. 3.1). The resulting models of trees were 9 m and 15 m tall with a diameter of 6 m and 8 m for *Tilia* × *vulgaris* and *Sorbus intermedia* respectively. A constant LAD value of 1.2 $\mathrm{m}^2\ \mathrm{m}^{-3}$ was set for the whole crown for both species. This value is a conservative estimate for broad-leaved trees (Abhijith et al., 2017), however it is not specific for street trees in Helsinki. For one scenario small hedge rows were placed near the traffic lanes. These were represented as continuous media with a height of 0.75 m and a width of 1 m. A higher LAD value of 2.0 $\mathrm{m}^2\ \mathrm{m}^{-3}$ was used for the hedges (Abhijith et al., 2017).

Finally, the five vegetation scenarios were formed by inserting these individual plant elements into the built environments. In the scenario with the 58 m wide city boule-

vard (referred to as S1), four adjacent rows of *Tilia* × *vulgaris* were placed in the street canyon. For the first scenario with the 54 m wide city boulevard (S2A), three rows of *Tilia* × *vulgaris* were used. Scenario S2B was made otherwise identical to S2A, but continuous hedge rows were placed underneath the outermost tree rows. Scenario S2C had the same three-row tree configuration as S2A, but with the outermost tree rows consisting of *Sorbus intermedia* trees. In the scenario with the narrowest street canyon (50 m, hereafter S3), two *Tilia* × *vulgaris* rows were used. Cross-sections of these vegetation scenarios and the vegetation-free reference scenario (S0) together with the placements of the traffic lanes are illustrated in Fig. 3.2. A three-dimensional model of S2A with main and subdomain extents for WD = 8° highlighted is illustrated in Fig. 3.3.

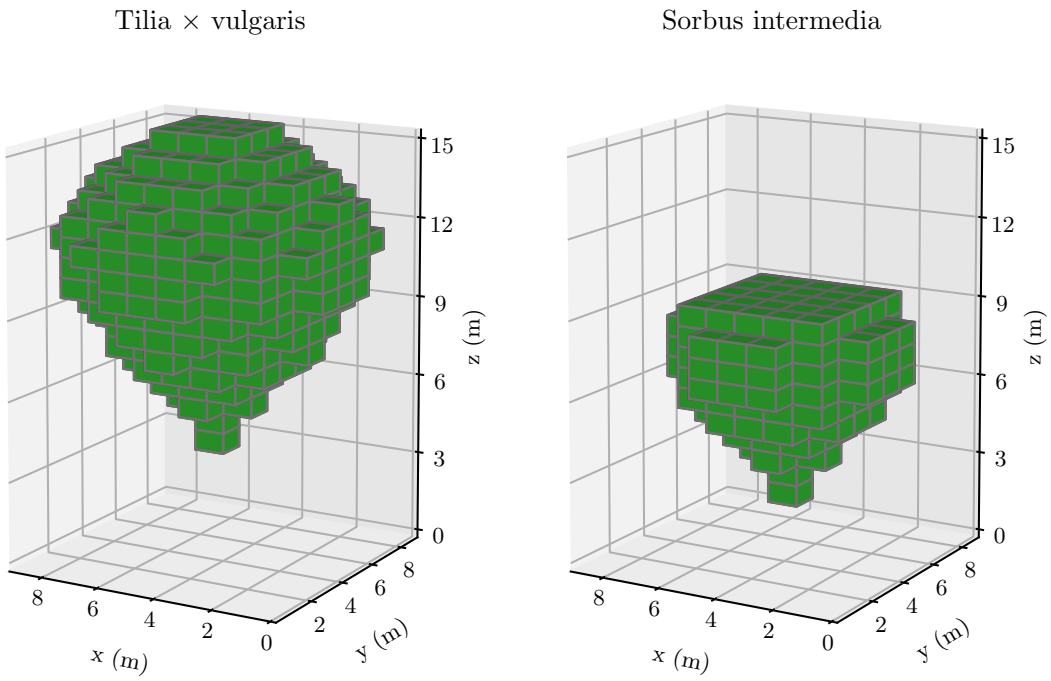

Figure 3.1: The three-dimensional models for *Tilia* × *vulgaris* and *Sorbus intermedia* trees constructed from the ALS inventory.

3.2.3 Aerosol emissions and boundary conditions

Aerosol emissions were considered as an area emission comprising of the traffic lane area within the city boulevard (see Fig. 3.2). To calculate the area emission, average unit emission factors for both $PM_{2.5}$ and PM_{10} for year 2030 were needed together with a traffic rate estimate for the city boulevard.

The average unit emission factor, i.e., the average emission of a given air pollutant from a single vehicle per unit transport distance, for $PM_{2.5}$ was estimated using the LIPASTO

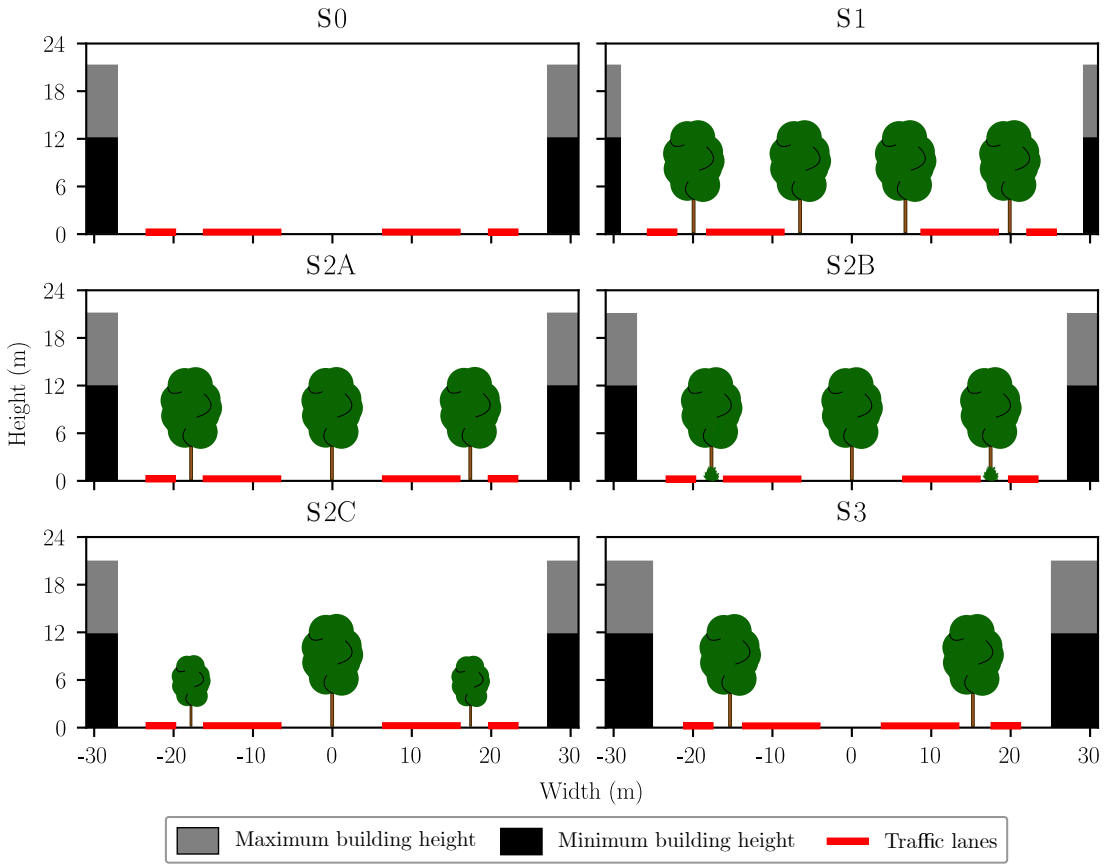

Figure 3.2: An illustrative diagram of the cross-sections of the vegetation scenarios used in this study. The shapes and sizes of the tree crowns are referential. Note the positioning of low hedge rows beneath outermost tree rows in S2B.

unit emissions database by VTT (2018b). In the LIPASTO database the unit emissions are given separately based on vehicle type, motive power used by vehicle and European emission standard (Euro). These standards are used to limit the exhaust emissions of new vehicles sold in European Union and European Economic Area (European Union, 2007 and subsequent amendments). LIPASTO also provides unit emission factors separately for motorway (typical traffic in Finnish motorways) and urban traffic (on average three full stops per kilometre with 30 km/h used as an average speed). Urban values were used in this study as it was viewed to better reflect the traffic on a city boulevard.

The vehicle fleet for 2030 was estimated using ALIISA vehicle fleet model for Finland, which is a sub-model of the LIPASTO calculation system (VTT, 2018a). ALIISA is a baseline model which takes into account already agreed policies on emission reductions, but does not include the effect of possible future policies. ALIISA provides an estimated share of road traffic mileage individually for each Euro standard and motive power type up to 2030. Additionally, the share between vehicle types (81% passenger cars, 10% vans, 6% buses, 3% trucks) was estimated based on vehicle counts in Mäkelänkatu, Helsinki, a street to which the Tuusulanväylä city boulevard is intended to end in the south (personal

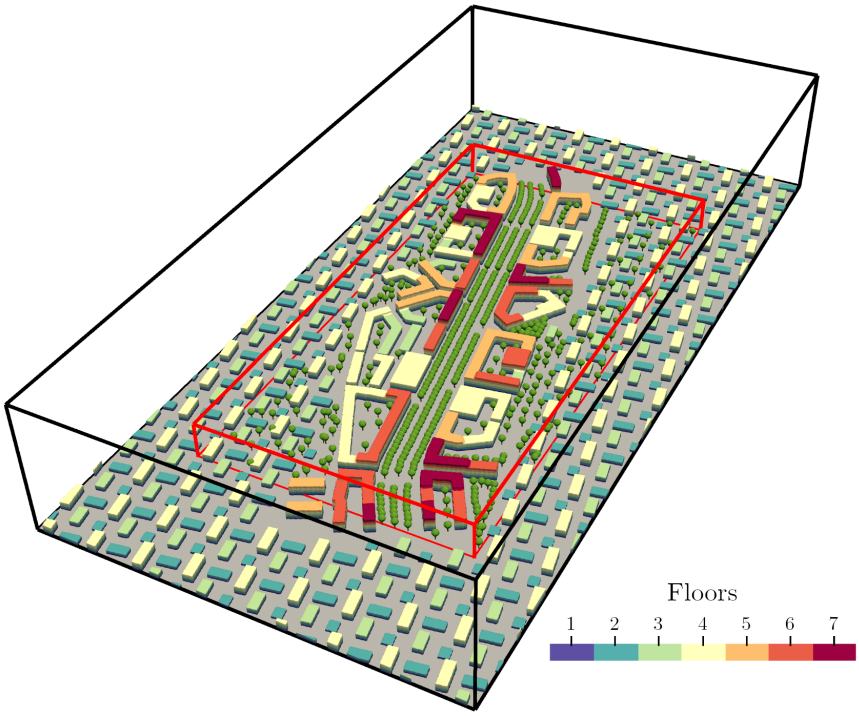

Figure 3.3: A three-dimensional representation of the scenario S2A with main and subdomain extents for WD = 8° highlighted in black and red respectively. The nearest boundary of the main domain is the inlet boundary for flow.

communication with the City of Helsinki on Oct 5, 2018). These shares were used as weights to compute a weighted average of the unit emission factors in LIPASTO database. An emission factor of $EF_{PM_{2.5}} = 3.18 \times 10^{-7}$ g m^{-2} s^{-1} was computed based on the vehicle fleet weighted unit emission, estimated traffic rate of 3660 veh h^{-1} and the total width of the motor traffic lanes (24 m) in the simplified city boulevard plan.

Unlike $PM_{2.5}$, majority of PM_{10} emissions from traffic in Helsinki originate from non-exhaust sources, composing primary of street dust (HSY, 2019). PM_{10} is particularly problematic in the springtime, when studded tires and residual from the wintertime sanding wear out dry paved surfaces (Kupiainen et al., 2013). The emission of street dust for dry late spring condition was estimated using data from the FORE road dust model, based on model runs done in Helsinki for years 2007–2009 and 2014 (Kauhaniemi et al., 2011). Data for morning rush hours (7–9 am) in April-May with applicable meteorological conditions were used. Hours with non-zero accumulated precipitation and mean horizontal wind speed below 3.3 m s^{-1} or above 6.3 m s^{-1} were filtered out from the FORE data before a 75-percentile value used as the unit emission factor for PM_{10} was calculated. The meteorological filtering was done in order to better match the wind conditions in the simulations (see Section 3.2.4) and to remove the effect of wet deposition to the street dust emission. Data from Kaisaniemi meteorological station in Helsinki was used in the meteorological filtering (Finnish Meteorological Institute, 2018b). As for $EF_{PM_{2.5}}$, the

total emission factor of $EF_{PM_{10}} = 1.7 \times 10^{-5}$ g m^{-2} s^{-1} was computed based on the unit emission, estimated traffic rate and the total width of the motor traffic lanes. For SALSA the emission factors were further translated to number emissions using a tri-modal log-normal aerosol size distribution based on SMPS measurements by Xue et al. (2015) for vehicle exhaust and distribution suggested by Zhang et al. (1999) for coarse particles.

Background concentrations for the SALSA model were calculated based on measurements in an urban background air quality measurement site in Kallio, Helsinki (Finnish Meteorological Institute, 2018a). These were calculated as the mean values for the morning rush hours for April–June 2008–2018, using the same filtering based on meteorological conditions that was used for PM_{10} emission factor calculation. The calculated values were $PM_{2.5} = 5.4$ µg m^{-3} (standard deviation $\sigma_{PM_{2.5}} = 3.4$ µg m^{-3}, $\min(PM_{2.5}) = 2.1$ µg m^{-3}, $\max(PM_{2.5}) = 19.5$ µg m^{-3}) and $PM_{10} = 17.4$ µg m^{-3} ($\sigma_{PM_{10}} = 11.5$ µg m^{-3}, $\min(PM_{10}) = 6.0$ µg m^{-3}, $\max(PM_{10}) = 61.2$ µg m^{-3}). These values were then used to construct a number concentration distribution with a similar shape as used by Zhang et al. (1999) for urban conditions and the resulting distribution was used as boundary conditions for the SALSA model. Furthermore, the aerosol size distributions of both emissions and background concentrations were divided into ten size sections, namely bins, to be used with the SALSA model. The aerosol size distributions and bin ranges are visualised in Fig. 3.4.

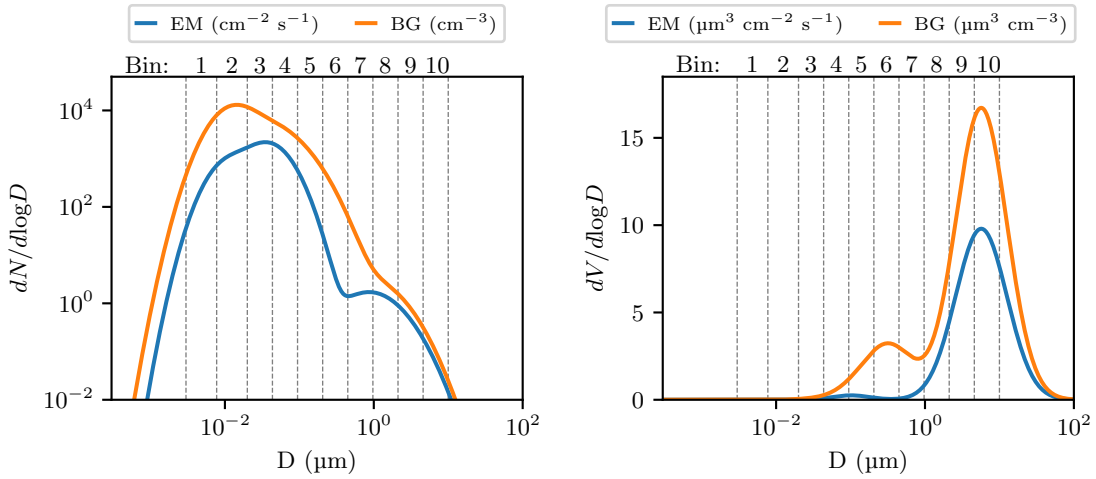

Figure 3.4: The aerosol number (left plot) and volume density (right plot) distributions for the emissions (EM, orange) and background concentrations (BG, blue). The ranges of aerosol size bins used in SALSA are visualised in grey dashed lines. Bins 1-4 correspond to $PM_{0.1}$, 1-8 to $PM_{2.5}$ and 1-10 to PM_{10}.

3.2.4 Model steering and computational setup

All vegetation scenarios were simulated using two wind directions: WD = 8° (referred hereafter as the parallel wind) and WD = 82° (perpendicular wind), given as an angle between the wind direction and street canyon. Slightly slanted wind directions were chosen

in order to avoid simulating extreme scenarios as well as to avoid in-place locking of unphysical turbulent structures described by Munters et al. (2016).

PALM's nesting functionality was utilised in the study by embedding a finer-grid subdomain within a coarser-grid main domain. Two 1152 m $\times$ 576 m main domains, one for each wind direction, were extracted from the original topography and vegetation data. Then, a smaller 768 m $\times$ 384 m subdomain covering was extracted from the main domain. A uniform grid resolution of 3 m was used for the main domain and 1.0 m horizontal and 0.75 m vertical resolutions used for the subdomain. The resulting morphometric properties of the domains and various areas of interest are presented in Table 3.1.

Estimating the inlet wind profile in such manner that the flow is immediately in balance with the surface friction can be difficult. The imbalance between the flow and the surface friction causes an IBL to form within the simulation. This IBL has to then fully develop and replace the original BL in order for the flow to reach a quasi-stationary state, which can take plenty of time depending on the initial guess (Andren et al., 1994). In order to minimise this time in the main simulations and to subsequently save computational resources, one precursor run was used to produce a mean inflow boundary condition for and the initial turbulent flow field for all the simulations. The precursor was run for six hours in simulation time, with a grid equal to the main domain in the main simulations. The same topography as for the suburban roughness in the main simulations was used in the precursor run in order for the inflow wind profile to represent one that would be caused by the roughness elements surrounding the area of interest.

The turbulent part of the inflow boundary condition was obtained using a turbulence recycling method with a recycling plane placed downstream the area of interest. Periodic boundary conditions were used at the spanwise boundaries, with Neumann boundary condition at the top of the domain. The flow boundary conditions of the nested subdomain were obtained from the main domain through the one-way nesting functionality.

The aerosol module SALSA was only used in the nested subdomain to reduce computational costs. Aerosol processes were limited to dry deposition, which was computed with a time step of $\Delta t_{\mathrm{SALSA}} = 1.0$ s for an aerosol size distribution represented by ten size bins (see Fig. 3.4. Dirichlet boundary conditions using background concentrations (Section 3.2.3) as fixed boundary conditions were used in lateral and top boundaries for SALSA.

All the main simulations were run for 1 hr 10 mins, with data being collected from the last hour. Simulations were performed on Cray XC40-based Sisu supercomputer located in Kajaani, Finland, operated by the CSC - IT Center for Science. For the parent domains and for the precursor run a 4 $\times$ 2 processor grid was used and a 24 $\times$ 12 grid was used for nested subdomains. Sisu consisted of Intel Xeon E5-2690v3 Haswell microarchitecture processor cores, with 24 cores per computation node.

Table 3.1: Morphometric properties of modelling domains and built areas used in the study. $H_{b,avg}$, $H_{b,min}$, $H_{b,max}$ are the average, the minimum and the maximum building height respectively, λ_p is the plan area fraction and λ_f is the frontal area fraction within the given area.

Area	$H_{b,avg}$ (m)	$H_{b,min}$ (m)	$H_{b,max}$ (m)	λ_p	λ_f
Main domain (WD = 8°)	10.3	4.0	21	0.34	0.19
Main domain (WD = 82°)	9.6	4.0	21	0.35	0.23
Subdomain (WD = 8°)	12.7	4.0	21	0.33	0.20
Subdomain (WD = 82°)	10.4	4.0	21	0.35	0.23
Along the boulevard	17.2	12.0	21.0	-	-
Suburban area (WD = 8°)	8.2	4.0	12.0	0.36	0.18
Suburban area (WD = 82°)	8.2	4.0	12.0	0.36	0.23

3.3 Data analysis

3.3.1 Post-processing

As the PALM model system uses a staggered grid, all output variables were first linearly interpolated to the cell-centers of the grid. For convenience, the output fields were then rotated in such that the studied boulevard aligned with the grid. This was done by multiplying 2-dimensional xy-plane with a rotation matrix at every grid vertical level as

$$\begin{bmatrix} x_r \\ y_r \end{bmatrix} = \begin{bmatrix} \cos\theta & \sin\theta \\ -\sin\theta & \cos\theta \end{bmatrix} \begin{bmatrix} x \\ y \end{bmatrix}, \tag{3.6}$$

where $-\theta$ is the angle between the grid and the boulevard direction. For convenience, the rotated horizontal coordinates x_r and y_r are simply referred to as x and y hereafter.

Most of the analysis requires temporal averaging of the variables. In this study, the temporal means were computed for a 60-minute period, beginning 10 minutes (simulation time) after the simulation initialization and ending to the end of the simulation. An exception to this is the precursor run, where a 3-hour averaging period was used, beginning from 3 hours (simulation time) after the simulation initialization. Spatial averages are represented by volumetric and areal integrals which were approximated using the discrete grid output datasets as

$$\langle a \rangle\,(t,\ N_x,\ N_y,\ N_z) \approx \frac{1}{N_x N_y N_z} \sum_{i=1}^{N_x} \sum_{j=1}^{N_y} \sum_{k=1}^{N_z} a(x = x(i),\ y = y(j),\ z = z(k),\ t), \tag{3.7}$$

for volume averages, where N_x, N_y, N_z are the number of grid points in the respective dimension in the volume of interest, and as

$$\langle a \rangle_{z=h}\,(t,\ N_x,\ N_y) \approx \frac{1}{N_x N_y} \sum_{i=1}^{N_x} \sum_{j=1}^{N_y} a(x = x(i),\ y = y(j),\ z = h,\ t) \tag{3.8}$$

for areal averages. The volumes and areas of interest used varied in the analysis and are declared separately for every analysed quantity.

3.3.2 Description of air pollutant removal and ventilation

PM_{10}, $PM_{2.5}$ and $PM_{0.1}$ mass concentrations were investigated at pedestrian level, set to be at $z = 1.9$ m, equivalent to the second vertical grid point for scalars in the staggered grid. An area of interest covering the whole width of the street canyon was used. 10 % of the total length was excluded from both ends of the boulevard to provide safety margins to the edges of the subdomain. As the emissions and background concentrations were held the same in all the scenarios, the relative differences in pedestrian-level mass concentrations between scenarios could be used as a measure to describe the total air pollutant removal performance by the ventilation and the vegetation. Furthermore, dependencies of these mass concentrations on statistics describing the flow kinetics within the street canyon were studied. The dependency on the E_k, K and k within the street canyon was studied using temporal data averaged from three levels ($z = 1.9,\ 8.6$ and 14.6 m).

Additionally for WD = 82°, for which the recirculation within the street canyon can strongly affect the air pollutant removal, a volumetric flow rate of the mean air circulation within the street canyon was computed. Stream function for two-dimensional flow is (Tritton, 1988)

$$\Psi = \int_A^P (u_i \,\mathrm{d}y - u_j \,\mathrm{d}x). \tag{3.9}$$

Due to the conservation of mass and subsequent conservation of volume due to fluid incompressibility assumption used, this can be defined as

$$\overline{\Psi(x,z)} = \int_0^z \frac{1}{y_2 - y_1} \int_{y_1}^{y_2} \overline{u}(x,y,z) \,\mathrm{d}y \,\mathrm{d}z, \tag{3.10}$$

where y_1 and y_2 represent the y-coordinates of the beginning and the end of the city boulevard respectively. The simplification is based on the assumption that no volume of air can be lost in the mean circulation, thus making the integration in the x-direction redundant. This is not actually the case in the environment we have at hand, because some air can escape or flow in through the cross streets joining with the city boulevard. However, the effect of this on the temporal mean value of Ψ is approximated to be negligible. The absolute value of the stream function at a given point (x, z) gives the volumetric flow rate along axis x below height z per unit length along axis y. The absolute value of the local minimum of $\overline{\Psi}$ within the street canyon ($\overline{Q} = \left|\min\left(\overline{\Psi}\right)\right|$) can be thus interpreted as the volumetric flow rate of the mean circulation within the street canyon, describing the mean recirculating flow within the canyon. These values were were used in the analysis as a measure of the magnitude of the air recirculation within the street canyon.

The dependencies of mean mass concentrations on the above-mentioned statistics were estimated using a linear regression model of the form $E\left[y(x)\right] = \beta_0 + \beta_1 x$, where y is

the mean mass concentration of interest, either PM_{10}, $PM_{2.5}$ or $PM_{0.1}$, and x is the explanatory variable of interest. Regression coefficients β_0 and β_1 were estimated from the simulated values of x and y for each scenario using the least-squares method. Furthermore, the confidence interval of the model was estimated using the bootstrap method, where the original data is resampled with replacement from the original sample. In case of bootstrapping linear regression, new samples of data are simulated by resampling the residuals of the original model (Efron and Tibshirani, 1986).

3.3.3 Quadrant analysis of vertical momentum flux

To further identify the possible changes in the behaviour of turbulence, the vertical transport of momentum was evaluated by vertical fluxes computed at a plane over the city boulevard. This plane was selected due to its location near the shear layer at roof top height, possibly allowing to identify the events when the shear layer is penetrated. The plane was positioned at $z = 23.6$ m, with flux values computed for every horizontal grid point within the area of interest at a 1 Hz sampling frequency. The area of interest was selected to cover the whole boulevard by length and width plus 10 m of extra width on both sides.

A quadrant analysis for the flux samples was performed following the analysis of Reynolds stress in a canopy layer by Shaw et al. (1983). The aim of the quadrant analysis is to classify the events or samples causing the vertical transport of momentum by dividing the temporal data of velocity variations into four categories based on a location of the sample in a Cartesian plane. The vertical kinematic Reynolds stress (Eq. (2.21)) of wind component u_i is divided into four quadrants defined as

$$\begin{aligned} \text{quadrant I:} \quad & u_i' > 0,\ u_k' > 0 \text{ (outward interaction)}, \\ \text{quadrant II:} \quad & u_i' < 0,\ u_k' > 0 \text{ (burst or ejection)}, \\ \text{quadrant III:} \quad & u_i' < 0,\ u_k' < 0 \text{ (inward interaction)}, \\ \text{quadrant IV:} \quad & u_i' > 0,\ u_k' < 0 \text{ (sweep or gust)}, . \end{aligned} \tag{3.11}$$

Thus the quadrants are effectively defined by their bounding two half-axes. Quadrants one and three contribute to the upward transport of momentum whilst quadrants two and four contribute to the downward transport of momentum. The total contribution to the transport of momentum during the observation period by a given quadrant can be calculated as a sum of individual flux samples falling into the given quadrant weighted by the sampling period. Furthermore, differences in the observed relative contributions between the scenarios were studied.

The Eq. (3.11) takes only one of the horizontal wind components into account. In effect, for three-dimensional flows, it is not possible to represent an individual flux sample on a two-dimensional plane directly. Thus, a coordinate transformation is performed to the flow field to get a better representation of the total vertical flux using just two wind

components. In this study, a two-dimensional coordinate rotation according to Kaimal and Finnigan (1994) is performed such that $\overline{u_i}$ is along the streamlines, $\overline{u_j} = 0$ and $\overline{u_k} = 0$.

For a visual reference, a theoretical distribution of the flux samples is fitted to the sample of velocity fluctuations. If velocity fluctuations in both vertical and horizontal directions follow a normal distribution, their bivariate data sample follows the multinormal distribution

$$f(\mathbf{y};\, \boldsymbol{\mu};\, \boldsymbol{\Sigma}) = (2\pi)^{-1} \det(\boldsymbol{\Sigma})^{-\frac{1}{2}} \exp\left(-\frac{1}{2}(\mathbf{y}-\boldsymbol{\mu})^T \boldsymbol{\Sigma}^{-1}(\mathbf{y}-\boldsymbol{\mu})\right), \tag{3.12}$$

where $\boldsymbol{\mu}$ is the mean vector, $\boldsymbol{\Sigma}$ is the covariance matrix and $\mathbf{y}$ is the bivariate data matrix (Rencher and Christensen, 2012). This method has the benefit of obtaining means, variances and the covariances for the variables using the maximum likelihood principle, simultaneously providing a probability density distribution for the visual analysis of the flux samples.

4 Results

4.1 Simulation diagnostics

In order to study the suitability of the used simulation setup to produce realistic quasi-stationary flow for each scenario, various diagnostics from the simulations were recorded. Final profiles of the horizontal wind speed and the ratio of the SGS vertical momentum flux from the total vertical momentum flux from the precursor run are presented in Fig. 4.1. A logarithmic profile is fitted to the wind profile to assess the aerodynamical roughness length corresponding to the suburban area surrounding the city boulevard and to evaluate how well the wind profile produced agrees with the theoretical profile. The fitted roughness length is $z_0 = 1.23$ m with a displacement height of $z_d = 5.79$ m. The ratio of the SGS and total fluxes is studied as in LES it is important that most of the turbulence is resolved and only a minor amount is modelled.

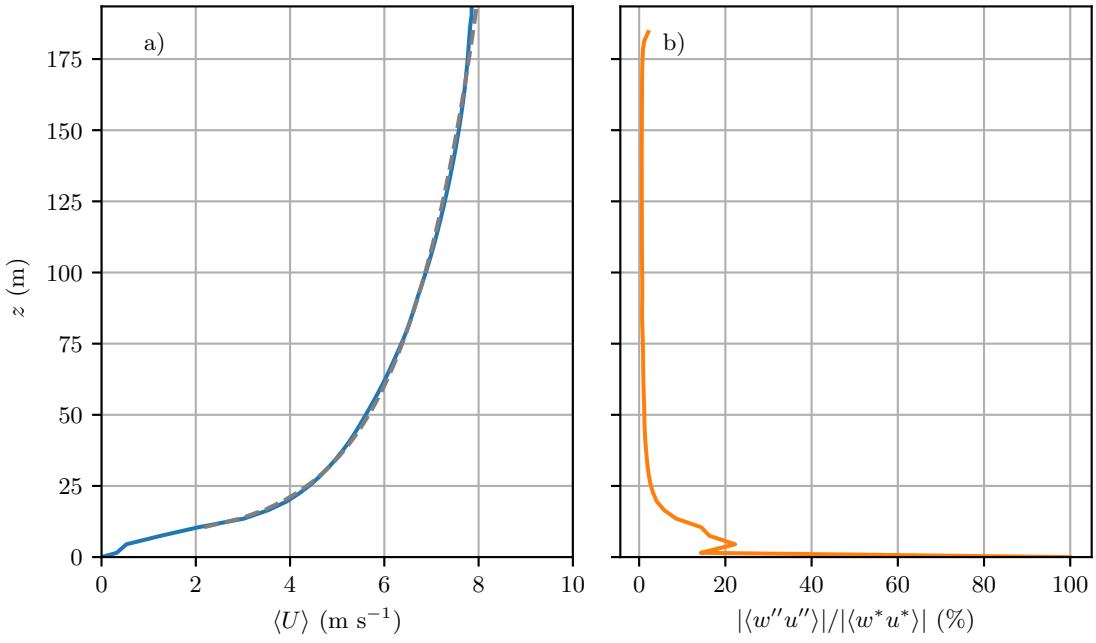

Figure 4.1: a) The vertical profile of the horizontal wind in the precursor run on blue solid line with a fitted logarithmic profile in grey. b) Vertical profile of the ratio of the vertical SGS momentum flux ($\langle w''u'' \rangle$) of the total vertical momentum flux ($\langle w^*u^* \rangle$).

The temporal evolution of spatially averaged wind profile ($\langle U \rangle_z$) and resolved-scale turbulence kinetic energy $\langle k^* \rangle_V$, presented in Fig. 4.2, are studied in order to assess if the

quasi-stationary state was achieved during the precursor run. $\langle k^* \rangle_V$ reaches its maximum value approximately at $t = 1800$ s, after which it nearly stabilizes at 0.50 $\mathrm{m^2 s^{-2}}$, with some oscillations remaining. The upper level winds take more time to stabilize than lower level ones, with winds at $z = 130$ m and 166 m showing a slight acceleration even at the end of the run.

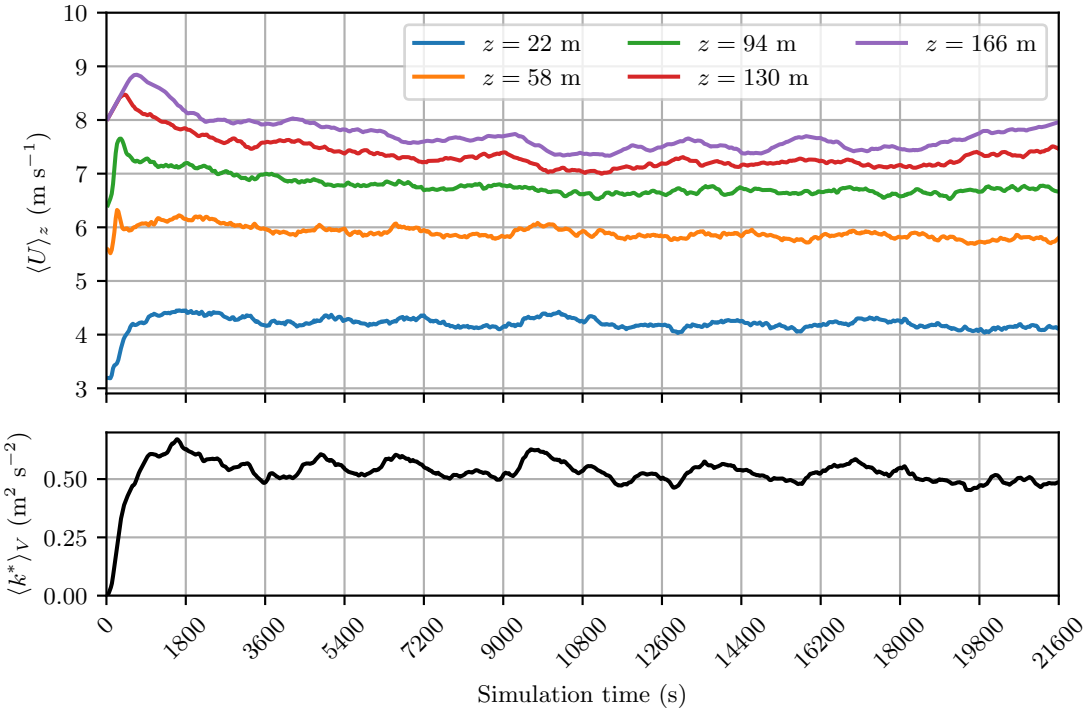

Figure 4.2: The time series of horizontal wind averaged over various levels ($\langle U \rangle_z$) and the average resolved-scale turbulence kinetic energy within model domain ($\langle k^* \rangle_V$) from the precursor run.

The evolution of the spanwise averaged wind profiles ($\langle U \rangle_y$) as the flow propagates through the simulation domain are studied in order to assess how well the flow is in balance with the surface friction, with the evolution in S0 with WD = 82° presented in Fig. 4.3. Ideally, if the inflow profile is in balance with the surface friction, no development of an IBL should occur near the inlet. For S0 and also for the other scenarios, small adjustment is observed near the inlet boundary ($x < 100$ m), with the profile quickly stabilising into a quasi-stationary state. The abrupt change in the lower level wind speeds corresponds to the location of the city boulevard, which has higher average building height than the surrounding suburban roughness.

4.2 Pedestrian-level aerosol mass concentrations

The simulated pedestrian-level aerosol mass concentrations, including their variability, are presented in Figs. 4.4 and 4.5 for WD = 8° and WD = 82° respectively, with numerical

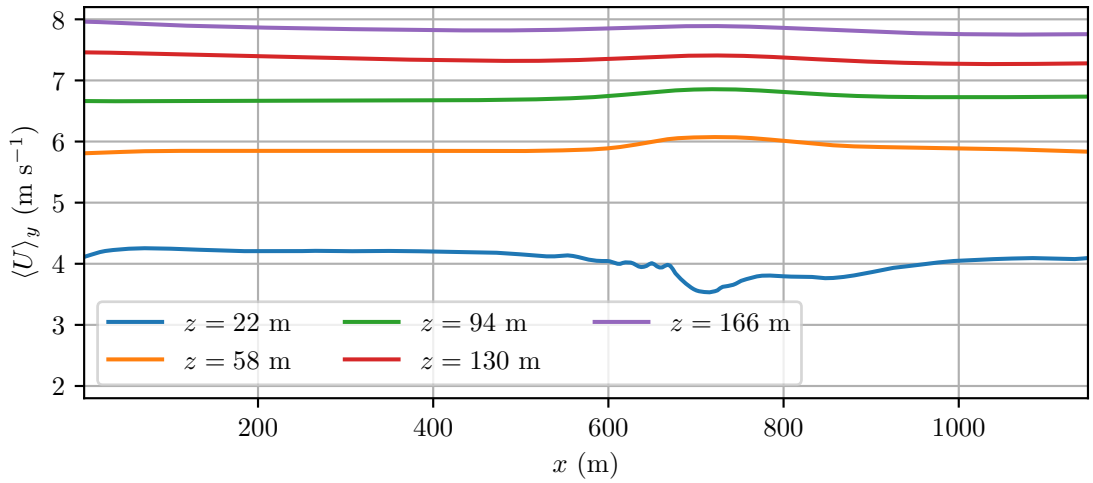

Figure 4.3: Evolution of mean wind speed at various levels in S0 with WD = 82° as a function of distance from the inlet boundary.

values presented in Tables A.1 to A.3 of Appendix A. In general, WD = 82° showed lower mass concentrations than WD = 8°. The scenario S0, i.e. the reference scenario without any vegetation, showed the lowest mean mass concentrations in all measures except for $PM_{0.1}$ with WD = 8°, where S2C showed 2 % decrease in mass concentration compared to S0. Overall, introduction of the street vegetation changed the mass concentrations compared to S0 by +12 to +54 %, +0 to +32 % and −2 to +33 % for PM_{10}, $PM_{2.5}$ and $PM_{0.1}$ respectively, with relative increases being higher in WD = 82°. In all scenarios and particle sizes, the 95th percentile values of the mass concentrations were higher in the scenarios with trees than in S0.

From the scenarios with vegetation, overall S2C performed the best in most measures. This is especially the case for WD = 8°, whilst for WD = 82° S2C performed the second best after S1. S1, however, does not perform well for WD = 8°, where it shows poor performances especially in terms of third quartile and 95th percentile values of the mass concentration. Introduction of hedges in S2B caused only small decrease (1% to 2%) in mass concentrations compared to S2A for WD = 8°, but for WD = 82° S2B showed higher (8% to 11%) mass concentrations than S2A.

The mean mass concentrations are additionally presented as a function of crown volume fraction (CVF) in Fig. 4.6 for both wind directions. A good correlation (R^2 = 0.93–0.75 depending on the particle size) between the mean pedestrian-level mass concentrations and the CVF can be observed for WD = 8°, with scenarios with a lower CVF showing lower mass concentrations. A better agreement is with the linear model is observed for PM_{10} than for the smaller particle sizes. For WD = 82°, a moderate correlation (R^2 = 0.52–0.48) is observed though without the vegetation-free scenario S0 the correlation would be significantly lower.

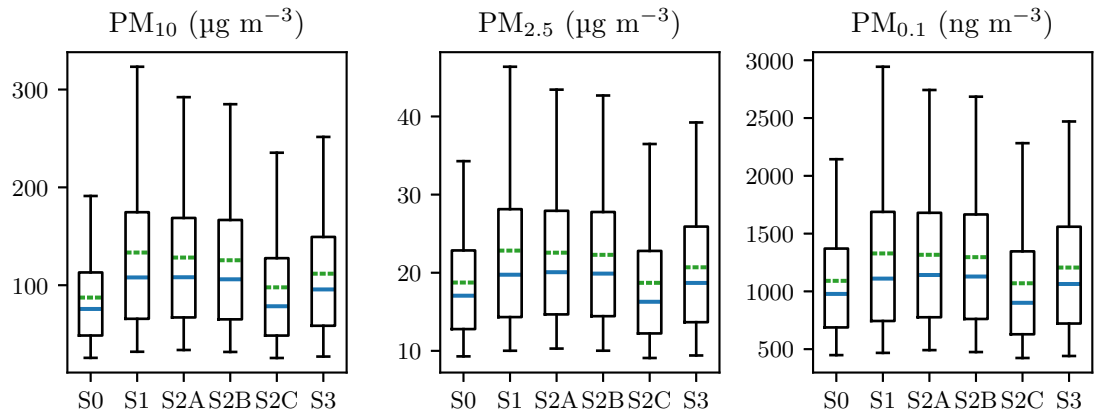

Figure 4.4: Boxplots of PM_{10}, $PM_{2.5}$ and $PM_{0.1}$ mass concentrations at pedestrian-level for simulations with WD = 8°. Temporal and spatial means and medians are marked with green dashed and blue solid lines respectively. Boxes signify the range between 1st and 3rd quartiles and whiskers the range between 5th and 95th percentiles.

4.3 Regression on flow kinetics

The dependency of the mean pedestrian-level PM_{10}, $PM_{2.5}$ and $PM_{0.1}$ mass concentrations on the average mean kinetic energy K, turbulence kinetic energy k and total kinetic energy E_k within the street canyon are illustrated in Figs. 4.8 and 4.9 for WD = 8° and WD = 82° respectively. For WD = 8°, the dependency of PM_{10} on E_k shows good agreement ($R^2 = 0.88$) with the linear model, with a decreasing dependency on E_k. Similarly to the dependency on CVF, the agreement with the linear model is not as good ($R^2 = 0.73$ and $R^2 = 0.69$) for the smaller particle sizes ($PM_{2.5}$ and $PM_{0.1}$). When examining the dependencies on K and k ($R^2 = 0.54$–0.36 and $R^2 = 0.22$–0.16 respectively), the agreement with the linear model is not nearly as good. The coefficients of determination are better for K than k, but mainly due to the existence of the vegetation-free scenario S0 in the data. With k, the linear model clearly fails to describe the differences in the mean mass concentrations.

For WD = 82° the results are quite different. The moderate values of R^2 (0.61–0.57) for the dependency of the mean mass concentrations on E_k can be mainly attributed to the vegetation-free scenario S0, with the linear model clearly failing to describe the differences otherwise. Interestingly, unlike for WD = 8°, the agreement of the data with the linear model is better with k as the independent variable in the model than with K ($R^2 = 0.61$–0.57 and $R^2 = 0.47$–0.45 respectively). However, in general the correlations in the data are quite small.

For WD = 82° the dependency of the mean mass concentrations on the volumetric flow rate of the mean circulation within the street canyon $\overline{Q}$ was also studied. The results, illustrated in Fig. 4.7, shows negative correlation with the mean mass concentrations and

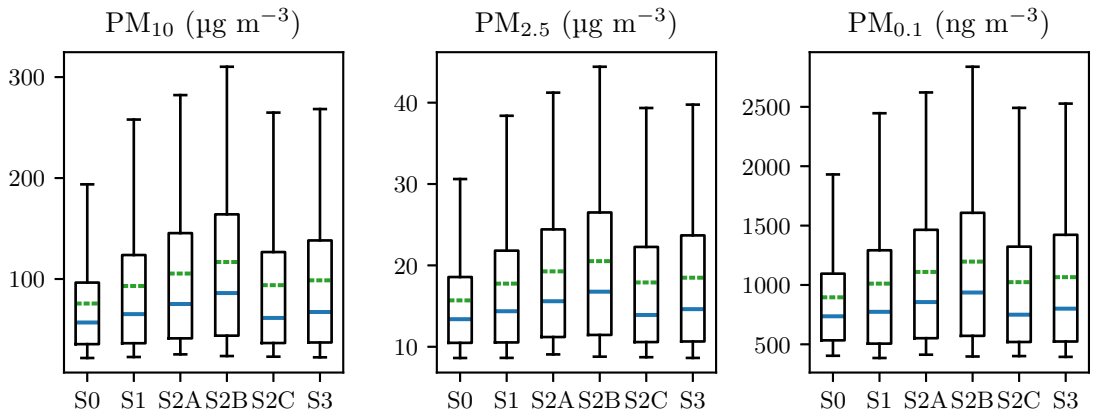

Figure 4.5: Boxplots of PM_{10}, $PM_{2.5}$ and $PM_{0.1}$ mass concentrations at pedestrian-level for simulations with WD = 82°. Temporal and spatial means and medians are marked with green dashed and blue solid lines respectively. Boxes signify the range between 1st and 3rd quartiles and whiskers the range between 5th and 95th percentiles.

$\overline{Q}$. The agreement of the model is not as good as with WD = 8° and E_k, but with values of R^2 between $0.64 - 0.67$ the agreement with the linear model is still at moderate level. Additionally, the fit is not completely driven by the vegetation-free scenario S0 unlike for kinetic energy measures, though much of it can still be attributed to it.

4.4 Quadrant analysis

The average momentum flux contributions above the street canyon at $z = 23.5$ m of each quadrant are pictured in Fig. 4.10 and Fig. 4.11 for WD = 8° and WD = 82° respectively. For WD = 8° the introduction of vegetation increases the net downward momentum flux for all scenarios (+73% to +93%) with an opposite but significantly smaller effect for WD = 82° (−4% to −14%). Quadrant III is slightly more significant (by 1 to 10 percentage points) for upward transport than quadrant I. For downward transport contributions by quadrants I and II are very closely equal to each other, except for S0 where a difference of 10 percentage points in the relative contribution is observed. Out of the scenarios including vegetation, S2C shows the highest average downward flux for both wind directions. The increase in turbulence kinetic energy within the street canyon for S3 does not reflect as an increase in downward momentum flux above the street canyon.

The distributions of the individual flux samples, presented in Appendix B in Figs. B.1 and B.2, in general follow the fitted bivariate normal distributions, with slight skewness observable in some scenarios. For WD = 8°, S2C stands out as it has much more outliers than what is predicted by the fitted distribution.

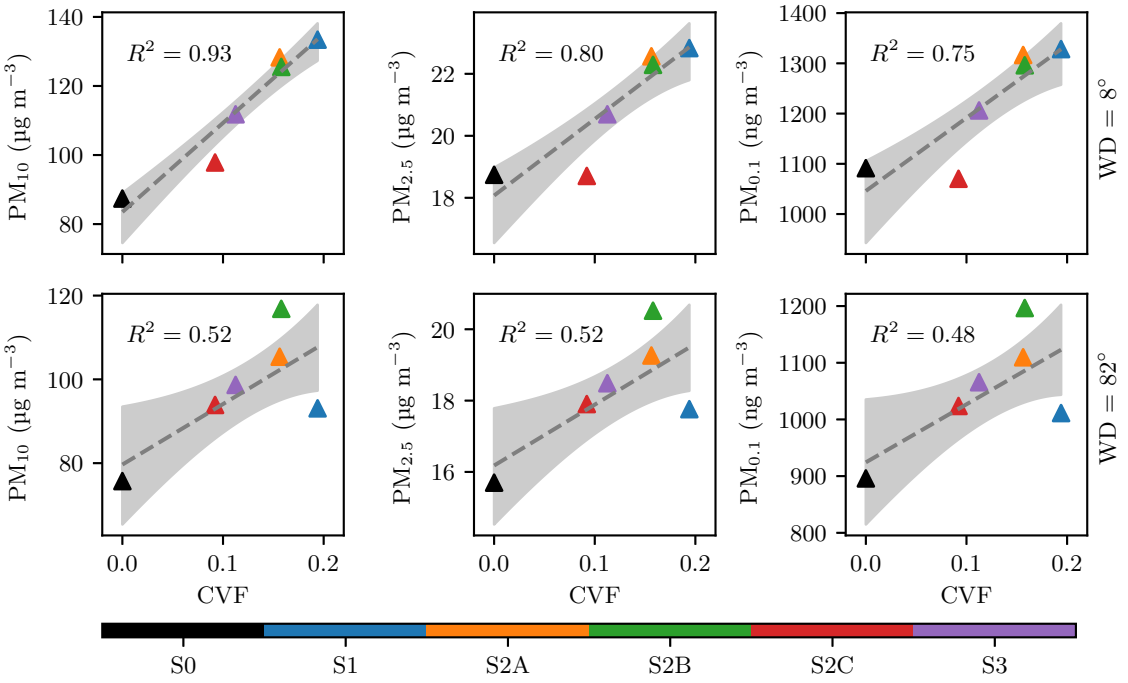

Figure 4.6: Scatter plots of mean PM_{10}, $PM_{2.5}$ and $PM_{0.1}$ mass concentrations at pedestrian-level as a function of CVF of the boulevard for WD = 8° in the upper and for WD = 82° in the lower panel. The gray dashed line shows the fitted linear model with the 95 % confidence interval shaded in light gray. The coefficient of determination R^2 is given individually for each fitted model.

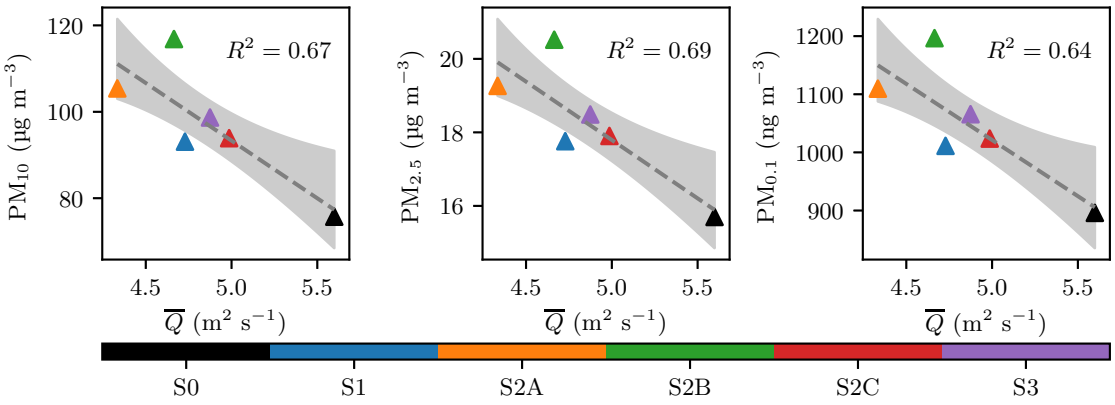

Figure 4.7: Scatter plots of mean PM_{10}, $PM_{2.5}$ and $PM_{0.1}$ mass concentrations at pedestrian-level as a function of the volumetric flow rate of the mean circulation within the street canyon $\overline{Q}$ for simulations with WD = 82°. The gray dashed line shows the fitted linear model with the 95 % confidence interval being shaded in light gray. The coefficient of determination R^2 is given individually for each fitted model.

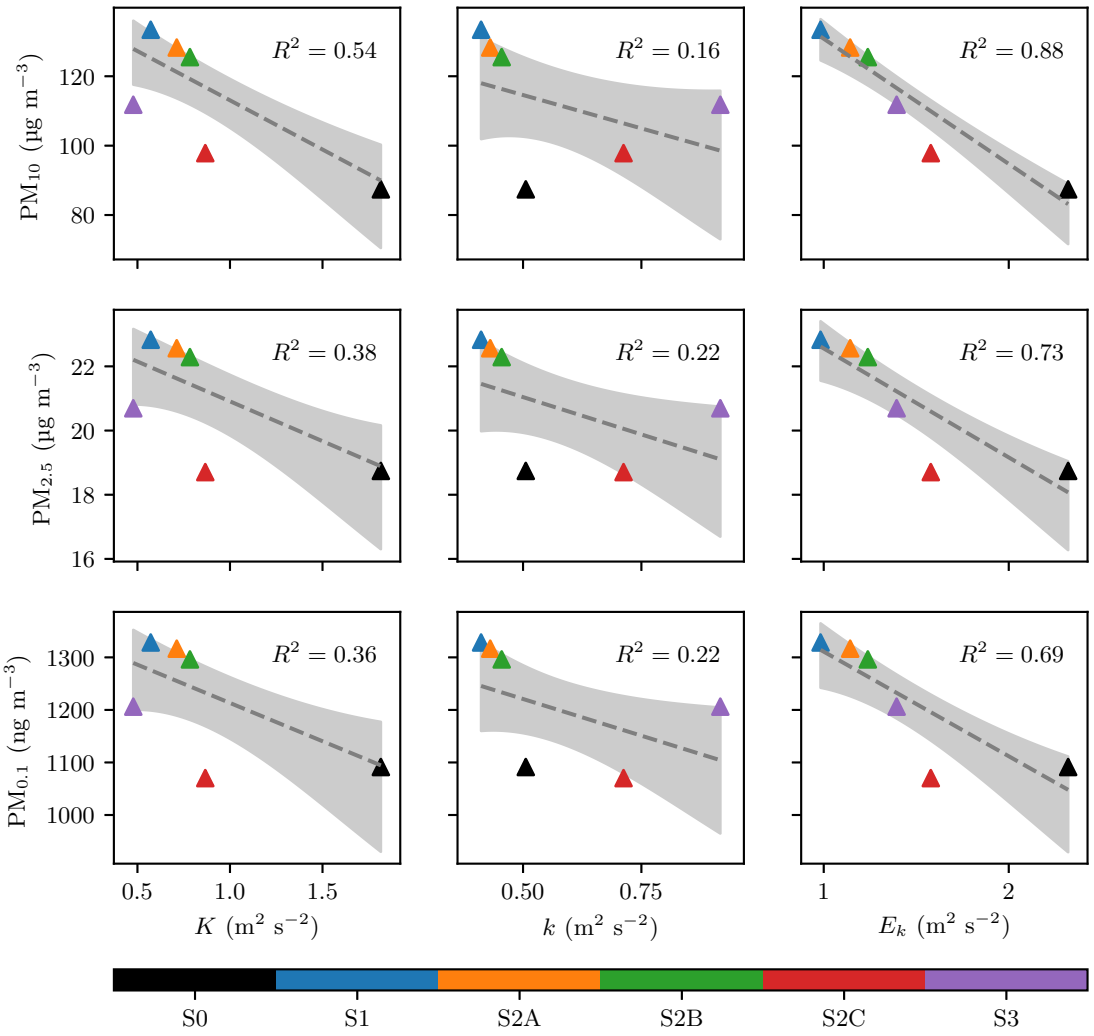

Figure 4.8: Scatter plots of mean PM_{10}, $PM_{2.5}$ and $PM_{0.1}$ mass concentrations at pedestrian-level as a function of average mean kinetic energy K, turbulence kinetic energy k and total kinetic energy E_k within the street canyon for simulations with WD = 8°. The gray dashed line shows the fitted linear model with the 95 % confidence interval of it being shaded in light gray. The coefficient of determination R^2 is given individually for each fitted model.

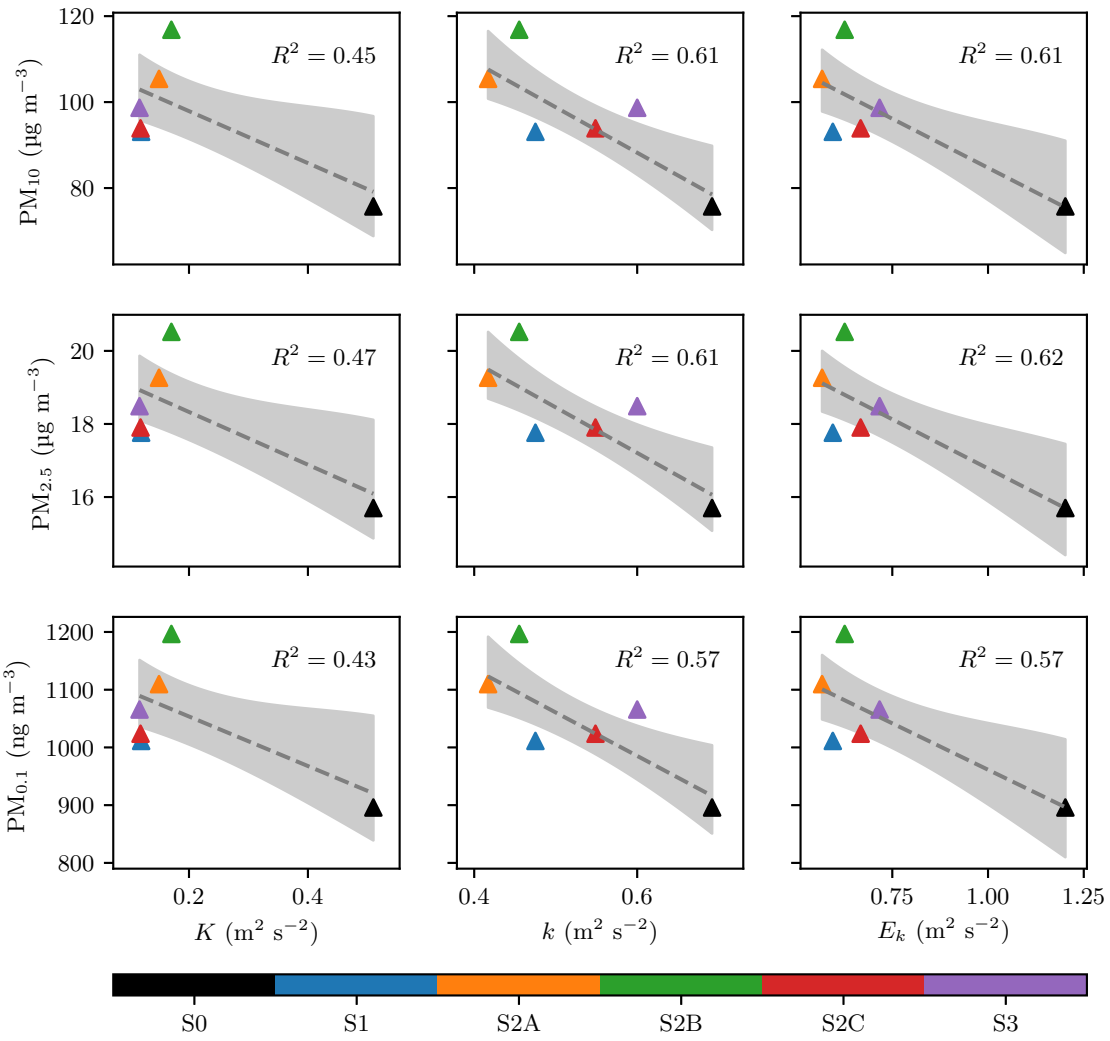

Figure 4.9: Scatter plots of mean PM_{10}, $PM_{2.5}$ and $PM_{0.1}$ mass concentrations at pedestrian-level as a function of average mean kinetic energy K, turbulence kinetic energy k and total kinetic energy E_k within the street canyon for simulations with WD = 82°. The gray dashed line shows the fitted linear model with the 95 % confidence interval being shaded in light gray. The coefficient of determination R^2 is given individually for each fitted model.

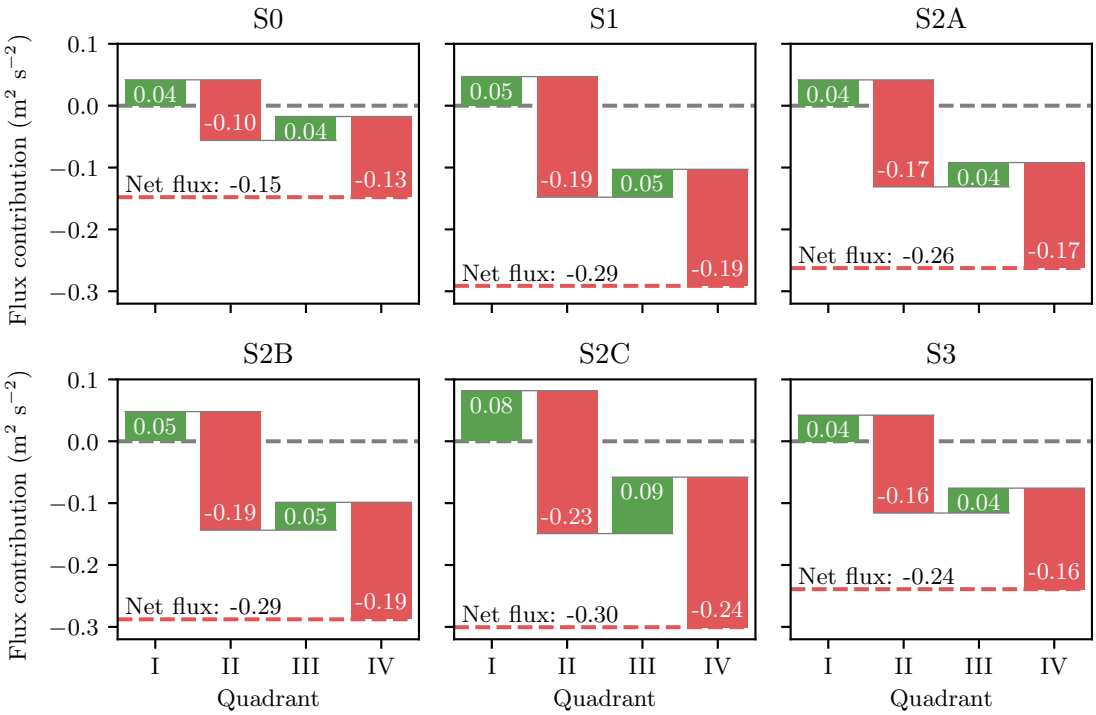

Figure 4.10: Mean net momentum fluxes and contributions of individual quadrants I-IV to it over the street canyon at $z = 23.5$ m for simulations with WD = 8°.

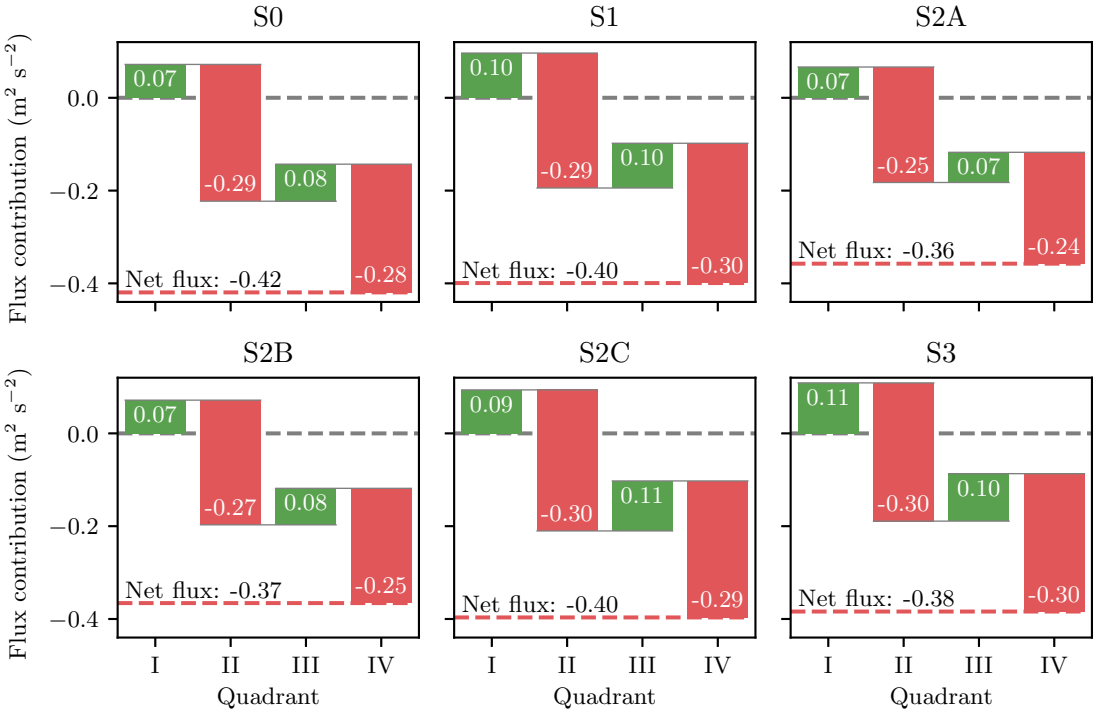

Figure 4.11: Mean net momentum fluxes and contributions of individual quadrants I-IV to it over the street canyon at $z = 23.5$ m for simulations with WD = 82°.

5 Discussion

5.1 Suitability of the simulation setup

The used simulation setup with a precursor run and turbulence recycling was able to produce a relatively quasi-stationary neutral flow conditions to the main runs. The simulations classify as LES since most of the vertical momentum flux was resolved and only small part modelled at SGS. Only at the first grid level the SGS fluxes dominated, but this is expected and unavoidable as the level is bounded by a no-slip wall below and the flow solution is dictated by the SGS wall model.

The resulting mean wind profile from the precursor run followed closely the fitted logarithmic profile as is expected for a neutral flow. The roughness length corresponding to the profile, $z_0 = 1.23$ m, is in a range of typical values for a suburban area (Hansen, 1993). It remains debatable whether the wind profile had converged fully during the six-hour precursor run as the upper levels experienced some acceleration at the end of the run. The effect of this on the simulation results is however likely to be very minimal, as the lower level wind velocities had converged well. The total resolved scale turbulence kinetic energy showed some fluctuations throughout the run, possibly due to inertial oscillations. These oscillations can be caused to a neutral flow by the imbalance between the pressure gradient force and surface friction (Andren et al., 1994). The oscillations are slowly damped by the friction as simulation proceeds which is somewhat visible from the time series, but some of the variance still remains at the end of the simulation run. However, in this case where only the mean wind profile is used from the precursor run, possible remaining inertial oscillations are unlikely to cause any difference for the final results, as the same inflow profile was used in all the simulations. The inflow mean flow profile derived from the precursor run proved to be a good match for the main simulations, as only a slight adjustment in the wind profile is observed near the inlet of the main domain, with the wind profile being well developed before air reaching the area of interest. Thus the simulation setup successfully created quasi-stationary neutral flow conditions while simultaneously saving computational resources by minimising the spin-up time required for simulating each scenario.

5.2 Pedestrian-level aerosol mass concentrations

The simulated pedestrian-level aerosol mass concentrations were high in comparison to guideline values set by WHO in all scenarios, especially for PM_{10} in scenarios including

vegetation. The simulations were set to replicate the conditions in a morning rush hour, whilst WHO guidelines are only for 24-hour and annual mean values. Estimating a 24-hour mean is not possible from the performed simulations and thus only qualitative comparison to the guideline values is possible. The 24-hour mean values would be significantly lower for the scenarios studied, as the mean traffic rate would be consequently lower than the mean traffic rate for a single morning rush hour used in the study. Although not fully comparable, the mean values observed in the simulations (75.7 to 133.4 µg m^{-3} and 15.7 to 22.8 µg m^{-3} for PM_{10} and $PM_{2.5}$ respectively) were approximately at the same levels as the highest 24-hour mean values (107 µg m^{-3} and 27 µg m^{-3}) measured in the street canyon of Mäkelänkatu, Helsinki in 2018 (HSY, 2019). Whilst no guideline values exist for $PM_{0.1}$, the observed mean values (896 ng m^{-3} to 1328 ng m^{-3}) were in the same order of magnitude as yearly mean value reported by Pakkanen et al. (2001) for Helsinki area between 1997-1997 (490 ng m^{-3}), albeit somewhat higher. Overall, the simulated pedestrian-level aerosol mass concentrations are in a credible range for what could be expected for a morning rush hour in a large street canyon.

The absolute differences in pedestrian-level mass concentrations observed between the scenarios could have significant implications for those exposed to the simulated conditions repeatedly. A study by Correia et al. (2013) estimated that a decrease of 10 µg m^{-3} in $PM_{2.5}$ mass concentration corresponds to a 0.35 years increase in mean life expectancy, with even stronger relation in urban areas. A study by Tecer et al. (2008) linked 10 µg m^{-3} increase in $PM_{10-2.5}$ mass concentrations with an 18% rise in children admitted to hospital due to asthma or respiratory diseases. A similar increase was found also due to increase in $PM_{2.5}$ mass concentrations. As the magnitudes of the absolute differences in the mean mass concentrations are significant in terms of health, comparing the relative differences between the scenarios becomes meaningful.

The observed relative differences in pedestrian-level mass concentrations between the scenarios including street trees (S1-S3) and the vegetation-free reference scenario (S0) had the same magnitude (-2 to $+54$ %) as the majority of the previous studies (Abhijith et al., 2017). By including also the effect of dry deposition, the simulations of this study further underline that the net effect of street trees on pedestrian-level mass concentrations is generally degenerative, with the reduction in ventilation having the dominant effect. An interesting observation is that the magnitude of the negative effect is smaller for the smaller particle sizes. This is an important finding in terms of the potential health effects, where especially the ultrafine particles can show a major negative contribution.

5.3 Effect on ventilation

A medium-to-high positive correlation was found between pedestrian-level aerosol mass concentrations and CVF. This indicates that the decrease in ventilation due to drag intro-

duced by the tree canopy is much more important in terms of pedestrian-level air quality than the dry deposition of particulates into the tree canopy. The correlation was the strongest for PM_{10} and lowest for $PM_{0.1}$, indicating an aerosol size dependency in the net effect. With WD = 8°, other scenarios lie quite within the confidence intervals of the fitted linear model, while S2C shows lower mass concentrations than what the linear model predicts, for all particle size ranges. This might be an indication of presence of a mechanism driving the ventilation that is not dependent on CVF or has a non-linear response to it.

Whilst CVF and pedestrian-level aerosol mass concentrations showed high correlation for WD = 8°, the correlation was not as strong for WD = 82° with more variability between the observed mass concentrations and linear model. This could be either due to a non-linear response of air pollutant ventilation to increased amount of vegetation in the street canyon, due to increase in the relative importance of dry deposition compared with WD = 8° or both. Comparing S2A and S2B, different only by the hedge rows next to traffic lanes introduced in S2B, gives an interesting insight to this matter. S2B show higher mass concentrations than S2A, which is unlikely to be caused by higher dry deposition in S2A as both scenarios have virtually the same CVF while S2B has added deposition surface area next to traffic lanes. Therefore the likely cause of higher mass concentrations in S2B is decreased ventilation near the street level due to added drag by hedge rows perpendicular to flow.

Significant differences in kinetic energies within the street canyon were also observed between the scenarios and wind directions. Perhaps the most interesting finding is that for WD = 8° the aerosol mass concentrations seem to depend quite linearly on E_k within the street canyon while the correlations with its components K and k are significantly weaker. This suggests that for winds parallel to the street canyon, the quality of the kinetic energy within the street canyon, if it is turbulent or steady, does not matter as much for the ventilation as the bulk magnitude of it. This is especially clear when comparing S0 and S3 with each other.

Out of the scenarios including vegetation, S2C shows the highest E_k. Introducing vegetation within the street canyon seems to promote the generation of turbulence in two scenarios: S2C and S3. S2C has the lowest CVF and thus impacts K compared with S0 the least and the increased k is able to compensate for some of the decrease in K. S3 shows an even higher increase in k, but with K lower than for any other scenario, E_k remains lower than for S2C. These findings suggest that even though the decrease in K by the vegetation seems somewhat unavoidable, this can be partially compensated by a vegetation configuration that promotes turbulence generation. Whilst it is not possible to say conclusively based on these results, the shear required for mechanical turbulence generation is probably higher in S2C due to the height variability of the vegetation canopy and in S3 due to increased spacing between the tree rows (28 m instead 16 m). Both potentially allow for more heterogeneity in wind velocities within the street canyon, thus

increasing shear and turbulence generation. Therefore vegetation configurations optimised for maximum shear could potentially be used in urban planning to counteract the negative effects of vegetation on ventilation.

For WD = 82° similar reasoning is not possible, with the regressed linear model on K being clearly not able to describe the aerosol mass concentrations: S0 drives the direction of the regressed model by its own. The same can be concluded also for E_k, but on k the medium correlation (R^2 = 0.61–0.57) observed might be justified. The correlations between the mass concentrations and $\overline{Q}$ are higher though much of it can still be attributed to S0. A conclusion that the aerosol mass concentrations are negatively correlated with the magnitude of the mean circulation would differ with some of the earlier studies suggesting that the ventilation with perpendicular wind is almost entirely driven by the turbulence and not by the magnitude of the recirculation (Cheng et al., 2008; Salizzoni et al., 2009). However, these studies did not take into account any vegetation, which might be able to redirect some of the flow in the recirculation through the shear layer out from the street canyon. Also, the slightly slanted wind direction used WD = 82° might be enough to break the decoupling of the recirculation from the flow above to some extent.

5.4 Quadrant analysis

The introduction of vegetation into the street canyon didn't affect the relative contributions of the quadrants, but rather scaled the overall momentum flux. This can be seen as a consequence of two factors: the distributions of flux samples closely followed the bivariate multinormal distributions for all scenarios and the covariances were similar in all cases. For WD = 8°, S3 had the highest increase in k compared to S0, with S2C having the second-highest increase. However, S2C showed higher increase in the net downward flux than S3 compared to S0. This might indicate that even though in S3 the trees are able to generate more turbulence within the street canyon than in S2C, it is not enough to penetrate the shear layer and to allow air to ventilate from the street canyon.

This conclusion is further supported by studying the distributions of individual flux samples, which show disproportionately large amount of outliers for S2C compared to what is predicted by the fitted distribution. This relative increase in outlier samples could possibly indicate the penetration of the shear layer. Events represented by these samples might produce the distribution observed for S2C, as occasionally large velocity fluctuations can be caused by the exchange of air between two flow regimes.

For WD = 82°, the differences between scenarios are small. Fluxes were calculated at z = 23.5 m, which is 6.3 m higher than average building height. Although the inspection area was set to exceed the width of the boulevard by 10 meters on both sides, the height of the layer might have been too high to catch interactions through the shear layer.

6 Conclusions

In this study, different vegetation scenarios that could be realistically used at the city boulevards were compared with an aim to understand which of the scenarios is the best in terms of their air pollutant removal performance. The air pollutant removal performance of the scenarios was studied using pedestrian-level aerosol mass concentrations. Furthermore, the dependency of the pedestrian-level aerosol mass concentrations on mean and turbulent flow statistics were studied. The suitability of the used LES setup with LES-LES self-nesting and turbulence recycling to produce quasi-stationary flow conditions for similar intercomparison dispersion studies was also studied.

Six vegetation scenarios were considered, with one being a vegetation-free reference scenario. The vegetation scenarios used were constructed on what was estimated to be realistic options for a city boulevard, with street trees being the prominent vegetation in all of them. Two wind directions, 8° and 82° with respect to the boulevard, and one wind speed were considered. A LES model PALM was employed to simulate the flow. A sectional aerosol model SALSA integrated into PALM was used to account for the behaviour of aerosol particles of different sizes, with the dry deposition of particles on built and leaf surfaces taken into account. Neutral and dry atmospheric conditions were used, with emissions and wind conditions estimated for a late spring morning. The pedestrian-level aerosol mass concentrations were computed for three different aerosol particle size ranges, PM_{10}, $PM_{2.5}$ and $PM_{0.1}$ to study the possible aerosol size dependency of the results.

In the LES setup, computational time was saved by minimising the time required for the flow to balance with the surface friction in each simulation using a combination of mean inflow boundary condition from a precursor run. A turbulent part was imposed on the mean inflow profile using turbulence recycling technique. The used setup successfully produced a quasi-stationary flow conditions for the simulations, providing similar flow conditions for all scenarios.

For all particle size ranges and scenarios, a significant increase in pedestrian-level aerosol mass concentrations was observed for the cases including vegetation compared with the vegetation-free scenario due to the decrease in ventilation of the street canyon. The relative aerosol mass concentration increases were higher for WD = 82° than for WD = 8° and the increases showed some dependency on particle size, being lower for smaller particles. Overall the differences in absolute values could have implications in terms of air quality and health effects for those exposed to air within the city boulevard regularly. Out of the realistic scenarios for the city boulevards, on average S2C showed

the lowest mass concentrations and S1 the highest.

The pedestrian-level aerosol mass concentrations were found to correlate with the portion of the street canyon volume occupied by the vegetation canopy. The correlation was strong for WD = 8° and PM_{10}, with WD = 82° and smaller particle size ranges showing medium to medium-high correlation. Furthermore, the mass concentrations in simulations with WD = 8° were found to have a strong negative correlation with the average total kinetic energy within the street canyon. While the inclusion of vegetation significantly decreased the mean kinetic energy of the flow, in some scenarios, namely S2C and S3, the increased spacing or height variability of the street tree rows were able to counteract some of the lost mean kinetic energy by increased turbulence kinetic energy. The increased spacing and/or height variability of the street trees can potentially allow for greater velocity differences within the street canyon, increasing mechanical turbulence generation. Inclusion of hedge rows were not found to have significant effect for WD = 8°, with a small increase for WD = 82°. For WD = 82° the correlations with the mass concentrations and flow kinetic energy were not as strong, with considerable discrepancy between the linear model and simulated data. A stronger correlation was found with the recirculating flow within the street canyon. This contradicts some of the previous studies on street canyon ventilation with perpendicular winds without vegetation. It is possible that street trees are capable of redirecting some of the flow in the recirculation through the shear layer and out from the street canyon, thus increasing the ventilation. However, no conclusive evidence of this is presented.

Studying individual flux samples above the street canyon using quadrant analysis suggests that even though street trees would be able to produce turbulence within the street canyon, it might not be enough to increase the frequency of samples where the shear layer located at building roof height is penetrated. For WD = 8° some evidence of these samples were found for scenario S2C, but not for S3, possibly due to better sheltering provided by buildings due to the narrower street width. For WD = 82° no clear conclusions could be drawn, as the differences between the scenarios were small. This could have been a result of a too high placement of the layer where the fluxes were studied. Thus, in order to get a more comprehensive picture of the structure of turbulence within and above the shear layer and better understanding on the interaction between the air within the street canyon and the air aloft, more data within and from close vicinity of the shear layer is required.

Based on the results, it is recommended to prefer variable-height street tree canopies similar to one in S2C within street canyons over uniform ones to compensate for the decreased wind speeds with increased turbulence. It is also recommendable to take the resulting CVF of the planned street canyon into account as the aerosol mass concentrations are generally higher in configurations with higher CVF. The results are applicable to the wide street type studied. More combinations of wind directions, wind speeds, street canyon morphologies and vegetation scenarios should be studied before more general conclusions can be made for urban planning.

The amount of scenarios studied was relatively low due to limited computational resources available combined with the heavy computational load of the LES model and the aerosol module, leaving some possible scenarios unexplored. However, using these computationally heavy methods was instrumental in this study, as the capabilities of lighter approaches are limited in complex urban environment. A more comprehensive study would therefore require significantly more computing resources. Further studies are required in order to gain better understanding about the processes affecting the street canyon ventilation, especially those taking place at the highly turbulent shear layer.

Acknowledgements

The simulations analysed in this study were originally performed for study described in the journal article *"Large-eddy simulation of the optimal street-tree layout for pedestrian-level aerosol particle concentrations – A case study from a city-boulevard"* (Karttunen et al., 2020). Although the analysis for this thesis is done independently from the original study, I wish to thank all the co-authors of the article[1] as they were instrumental in planning the original study and the simulation setups.

The City of Helsinki made this study possible by providing detailed information of the planned city boulevard, including possible vegetation scenarios and projected traffic rates. I would also like to thank M. Kauhaniemi from the Finnish Meteorological Institute for supplying the FORE model data as well as for the help analysing it.

Finally I wish to thank the supervisors of this thesis, M. Kurppa and L. Järvi, for their guidance and support throughout the project.

[1] M. Kurppa, M. Auvinen, A. Hellsten and L. Järvi

A Numerical values for pedestrian-level aerosol mass concentrations

Table A.1: Spatial and temporal means, medians, 1st and 3rd quartiles and 5th and 95th percentiles of PM_{10} mass concentrations (µg m^{-3}) at pedestrian-level ($z = 1.9$ m) for simulations with WD = 8°.

Scenario	WD	Mean	Median	$q1$	$q3$	$p5$	$p95$
S0	8°	87.4	75.7	48.6	113.1	25.8	191.2
	82°	75.7	56.9	35.5	96.5	21.8	193.8
S1	8°	133.4	108.0	65.7	174.6	32.0	323.2
	82°	93.1	65.2	36.4	123.8	22.7	258.0
S2A	8°	128.3	108.2	67.1	168.8	33.8	292.2
	82°	105.4	75.3	41.2	145.5	25.4	282.2
S2B	8°	125.5	106.1	65.1	166.7	31.8	285.0
	82°	116.8	86.1	43.9	164.1	23.7	310.3
S2C	8°	97.8	78.5	48.6	127.7	25.6	235.4
	82°	93.9	61.4	36.6	126.7	23.1	264.8
S3	8°	111.8	95.7	58.5	149.3	27.1	251.5
	82°	98.7	67.3	37.1	138.2	22.4	268.3

Table A.2: Spatial and temporal means, medians, 1st and 3rd quartiles and 5th and 95th percentiles of $PM_{2.5}$ mass concentrations (µg m^{-3}) at pedestrian-level ($z = 1.9$ m), given individually for both wind directions.

Scenario	WD	Mean	Median	$q1$	$q3$	$p5$	$p95$
S0	8°	18.7	17.1	12.8	22.9	9.3	34.3
	82°	15.7	13.4	10.5	18.6	8.6	30.6
S1	8°	22.8	19.7	14.3	28.1	10.0	46.3
	82°	17.8	14.4	10.5	21.8	8.6	38.4
S2A	8°	22.6	20.1	14.6	27.9	10.3	43.4
	82°	19.3	15.6	11.2	24.4	9.1	41.2
S2B	8°	22.3	19.9	14.4	27.7	10.0	42.7
	82°	20.5	16.8	11.5	26.5	8.8	44.4
S2C	8°	18.7	16.3	12.2	22.8	9.1	36.5
	82°	17.9	13.9	10.6	22.3	8.7	39.3
S3	8°	20.7	18.7	13.7	25.9	9.4	39.2
	82°	18.5	14.6	10.6	23.7	8.6	39.8

Table A.3: Spatial and temporal means, medians, 1st and 3rd quartiles and 5th and 95th percentiles of $PM_{0.1}$ mass concentrations (ng m^{-3}) at pedestrian-level ($z = 1.9$ m) for simulations with WD = 8°.

Scenario	WD	Mean	Median	$q1$	$q3$	$p5$	$p95$
S0	8°	1091.3	978.0	688.1	1370.5	448.5	2143.5
	82°	896.0	736.1	533.6	1095.2	403.9	1930.7
S1	8°	1328.4	1110.6	743.9	1688.2	467.9	2943.9
	82°	1011.3	773.8	505.9	1292.1	385.0	2446.1
S2A	8°	1316.6	1141.7	776.1	1680.1	491.8	2742.8
	82°	1109.7	856.0	551.6	1464.5	412.8	2621.3
S2B	8°	1296.2	1128.6	761.3	1665.8	475.1	2684.9
	82°	1196.6	936.4	571.5	1607.8	397.6	2837.7
S2C	8°	1070.2	901.2	628.8	1346.4	423.6	2282.5
	82°	1023.8	749.6	519.6	1322.6	401.1	2491.3
S3	8°	1206.3	1064.0	721.8	1559.6	440.9	2470.3
	82°	1065.7	800.4	523.7	1422.4	394.4	2527.3

B Scatter plots of flux samples

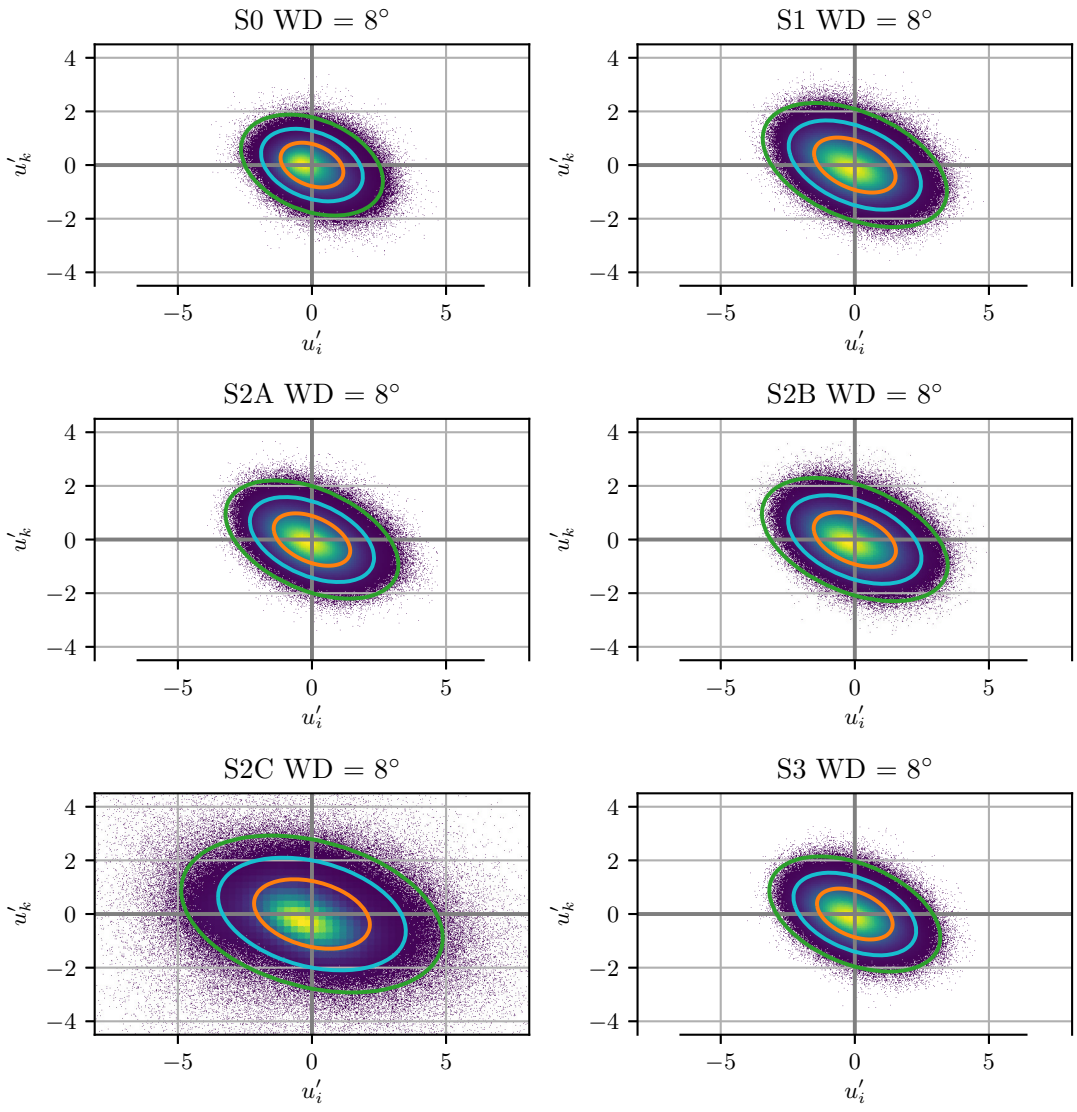

Figure B.1: Scatter plots of individual momentum flux events at $z = 23.5$ m for simulations with WD = 8°. The colour shading signifies the relative frequency of events for areas where multiple events overlap. The 99.7%, 95% and 68% confidence regions of a fitted bivariate normal distribution are enclosed with green, cyan and orange ellipses respectively.

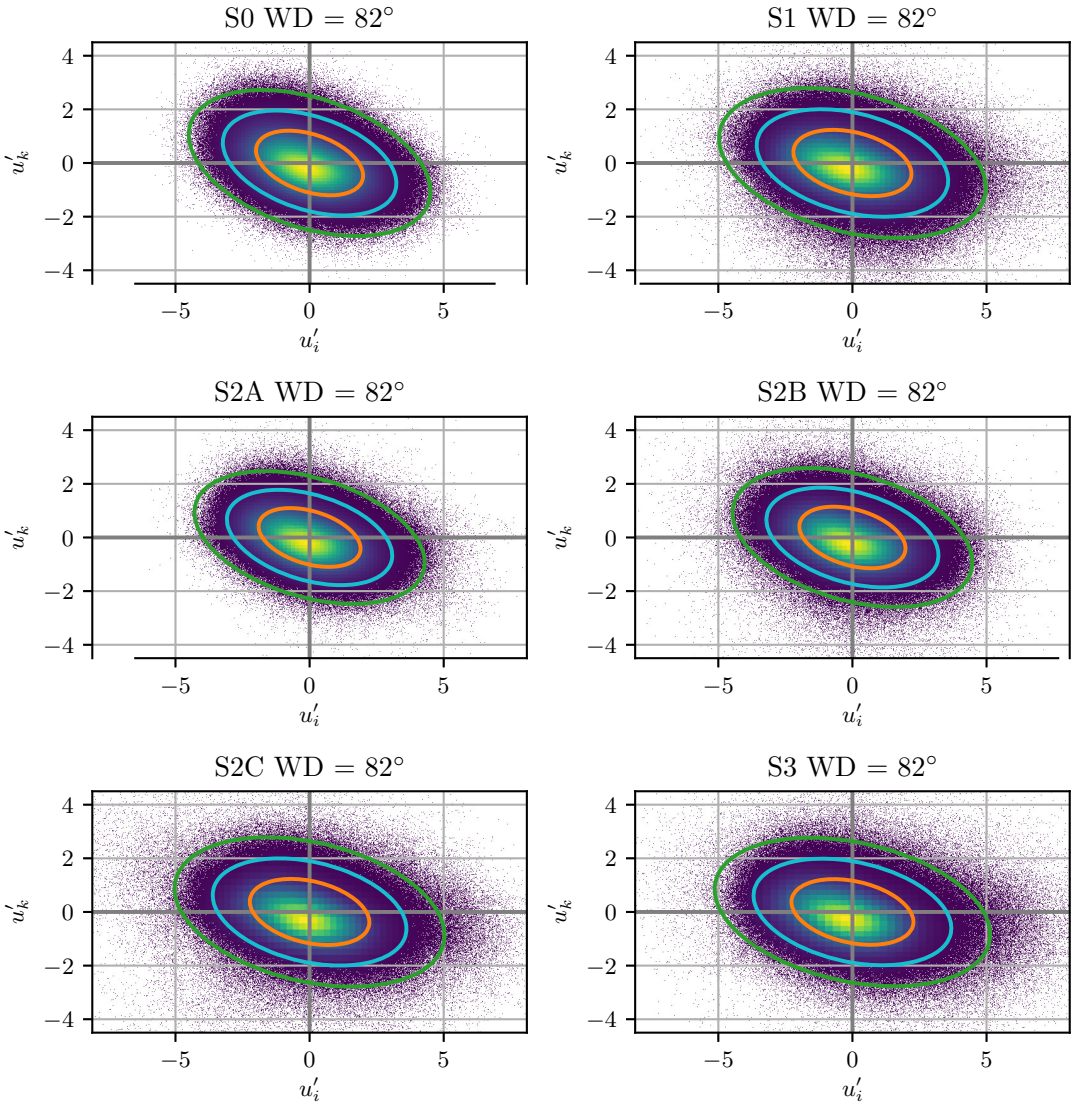

Figure B.2: Scatter plots of individual momentum flux events at $z = 23.5$ m for simulations with WD = 82°. The colour shading signifies the relative frequency of events for areas where multiple events overlap. The 99.7%, 95% and 68% confidence regions of a fitted bivariate normal distribution are enclosed with green, cyan and orange ellipses respectively.

Bibliography

Abhijith, K., P. Kumar, J. Gallagher, A. McNabola, R. Baldauf, F. Pilla, B. Broderick, S. D. Sabatino] and B. Pulvirenti, 2017: Air pollution abatement performances of green infrastructure in open road and built-up street canyon environments – a review. *Atmospheric Environment*, **162**, 71 – 86, doi:https://doi.org/10.1016/j.atmosenv.2017.05.014, URL http://www.sciencedirect.com/science/article/pii/S1352231017303151.

Albayrak, I., V. Nikora, O. Miler and M. T. O'Hare, 2014: Flow–plant interactions at leaf, stem and shoot scales: drag, turbulence, and biomechanics. *Aquatic Sciences*, **76 (2)**, 269–294, doi:10.1007/s00027-013-0335-2, URL https://doi.org/10.1007/s00027-013-0335-2.

Andren, A., A. R. Brown, P. J. Mason, J. Graf, U. Schumann, C.-H. Moeng and F. T. M. Nieuwstadt, 1994: Large-eddy simulation of a neutrally stratified boundary layer: A comparison of four computer codes. *Quarterly Journal of the Royal Meteorological Society*, **120 (520)**, 1457–1484, doi:10.1002/qj.49712052003, URL https://rmets.onlinelibrary.wiley.com/doi/abs/10.1002/qj.49712052003, https://rmets.onlinelibrary.wiley.com/doi/pdf/10.1002/qj.49712052003.

Auvinen, M., 2019: Rasterh3d v1.0. Zenodo, URL https://doi.org/10.5281/zenodo.2538074, doi:10.5281/zenodo.2538074.

Blazek, J., 2005: *Computational Fluid Dynamics : Principles and Applications.*, Vol. 2nd ed. Elsevier Science.

Cheng, H. and I. P. Castro, 2002: Near wall flow over urban-like roughness. *Boundary-Layer Meteorology*, **104 (2)**, 229–259, doi:10.1023/A:1016060103448, URL https://doi.org/10.1023/A:1016060103448.

Cheng, W., C.-H. Liu and D. Y. Leung, 2008: Computational formulation for the evaluation of street canyon ventilation and pollutant removal performance. *Atmospheric Environment*, **42 (40)**, 9041 – 9051, doi:https://doi.org/10.1016/j.atmosenv.2008.09.045, URL http://www.sciencedirect.com/science/article/pii/S1352231008008443.

Chung, T. J., 2002: *Computational Fluid Dynamics*. Cambridge University Press, doi:10.1017/CBO9780511606205.

City of Helsinki, 2016: Helsingin yleiskaava. *Helsingin kaupunkisuunnitteluviraston yleissuunnitteluosaston selvityksiä*, in Finnish.

City of Helsinki, 2017: 3D city model of the city of Helsinki. City of Helsinki, URL http://kartta.hel.fi/3d/mesh.

Correia, A. W., r. Pope, C Arden, D. W. Dockery, Y. Wang, M. Ezzati and F. Dominici, 2013: Effect of air pollution control on life expectancy in the united states: an analysis of 545 u.s. counties for the period from 2000 to 2007. *Epidemiology (Cambridge, Mass.)*, **24 (1)**, 23–31, doi:10.1097/EDE.0b013e3182770237, URL https://pubmed.ncbi.nlm.nih.gov/23211349.

Coutts, A. M., E. C. White, N. J. Tapper, J. Beringer and S. J. Livesley, 2016: Temperature and human thermal comfort effects of street trees across three contrasting street canyon environments. *Theoretical and Applied Climatology*, **124 (1)**, 55–68, doi:10.1007/s00704-015-1409-y, URL https://doi.org/10.1007/s00704-015-1409-y.

Dupont, S. and Y. Brunet, 2009: Coherent structures in canopy edge flow: a large-eddy simulation study. *Journal of Fluid Mechanics*, **630**, 93–128, doi:10.1017/S0022112009006739.

EEA, 2019: Air quality in Europe - 2019 report. European Environment Agency.

Efron, B. and R. Tibshirani, 1986: Bootstrap methods for standard errors, confidence intervals, and other measures of statistical accuracy. *Statist. Sci.*, **1 (1)**, 54–75, doi:10.1214/ss/1177013815, URL https://doi.org/10.1214/ss/1177013815.

Eliasson, I., B. Offerle, C. S. B. Grimmond and S. Lindqvist, 2006: Wind fields and turbulence statistics in an urban street canyon. *Atmospheric Environment*, **40 (1)**, 1–16, doi:https://doi.org/10.1016/j.atmosenv.2005.03.031, URL http://www.sciencedirect.com/science/article/pii/S1352231005002967.

European Union, 2007: Regulation (EC) No 715/2007 of the European Parliament and of the Council of 20 June 2007 on type approval of motor vehicles with respect to emissions from light passenger and commercial vehicles (Euro 5 and Euro 6) and on access to vehicle repair and maintenance information. *Official Journal of the European Union*, **171**.

European Union, 2008: Directive 2008/50/EC of the European Parliament and of the Council of 21 May 2008 on ambient air quality and cleaner air for Europe. *Official Journal of the European Union*, **51**.

Finnish Meteorological Institute, 2018a: Air quality observations of cities and industry, last access 24 september 2018. URL http://catalog.fmi.fi/geonetwork/srv/fin/catalog.search#/metadata/cf1b68b2-78d8-481c-9c2c-2b950214d477.

Finnish Meteorological Institute, 2018b: Weather observations: Kaisaniemi, last access 21 august 2018. URL http://catalog.fmi.fi/geonetwork/srv/eng/catalog.search#/metadata/228310f3-12a3-43f6-9949-7ee27dc9b047.

Garratt, J. R., 1992: *The Atmospheric Boundary Layer*. Cambridge University Press.

Gatski, T. B., M. Y. Hussaini and J. L. Lumley, 1996: *Simulation and Modeling of Turbulent Flows*. ICASE/LaRC Series in Computational Science and Engineering, Oxford University Press.

Giometto, M. G., A. Christen, P. Egli, M. F. Schmid, R. T. Tooke, N. C. Coops and M. B. Parlange, 2017: Effects of trees on mean wind, turbulence and momentum exchange within and above a real urban environment. *Advances in Water Resources*, **106**, 154 – 168, doi:https://doi.org/10.1016/j.advwatres.2017.06.018, URL http://www.sciencedirect.com/science/article/pii/S0309170817306486.

Hansen, F. V., 1993: Surface roughness lengths. *U.S. Army Research Laboratory Technical Report*.

Hinds, W. C., 1999: *Aerosol Technology : Properties, Behavior, and Measurement of Airborne Particles.*, Vol. 2nd ed. Wiley-Interscience, URL http://search.ebscohost.com.libproxy.helsinki.fi/login.aspx?direct=true&db=nlebk&AN=531512&site=ehost-live&scope=site.

Holton, J. R., 2004: *An Introduction to Dynamic Meteorology*, International Geophysics, Vol. 88. 4th ed., Academic Press, doi:10.1016/S0074-6142(04)80034-2.

HSY, 2016: Ilmanlaatu ja siihen vaikuttavat tekijät pääkaupunkiseudulla vuosina 2006 - 2015. *HSY publications*, in Finnish.

HSY, 2019: Ilmanlaatu pääkaupunkiseudulla vuonna 2018. *HSY publications*, in Finnish.

Hussein, T., A. Puustinen, P. P. Aalto, J. M. Mäkelä, K. Hämeri and M. Kulmala, 2004: Urban aerosol number size distributions. *Atmospheric Chemistry and Physics*, **4 (2)**, 391–411, doi:10.5194/acp-4-391-2004, URL https://www.atmos-chem-phys.net/4/391/2004/.

Jin, S., J. Guo, S. Wheeler, L. Kan and S. Che, 2014: Evaluation of impacts of trees on pm2.5 dispersion in urban streets. *Atmospheric Environment*, **99**, 277 – 287, doi:https://doi.org/10.1016/j.atmosenv.2014.10.002, URL http://www.sciencedirect.com/science/article/pii/S1352231014007791.

Kaimal, J. C. and J. J. Finnigan, 1994: *Atmospheric Boundary Layer Flows : Their Structure and Measurement*. Oxford University Press, URL http://search.ebscohost.com.libproxy.helsinki.fi/login.aspx?direct=true&db=nlebk&AN=169057&site=ehost-live&scope=site.

Karttunen, S., M. Kurppa, M. Auvinen, A. Hellsten and L. Järvi, 2020: Large-eddy simulation of the optimal street-tree layout for pedestrian-level aerosol particle concentrations – a case study from a city-boulevard. *Atmospheric Environment: X*, **6**, 100 073, doi:https://doi.org/10.1016/j.aeaoa.2020.100073, URL http://www.sciencedirect.com/science/article/pii/S2590162120300125.

Kastner-Klein, P., E. Fedorovich and M. Rotach, 2001: A wind tunnel study of organised and turbulent air motions in urban street canyons. *Journal of Wind Engineering and Industrial Aerodynamics*, **89 (9)**, 849 – 861, doi:https://doi.org/10.1016/S0167-6105(01)00074-5, URL http://www.sciencedirect.com/science/article/pii/S0167610501000745.

Katul, G. G., L. Mahrt, D. Poggi and C. Sanz, 2004: One- and two-equation models for canopy turbulence. *Boundary-Layer Meteorology*, **113 (1)**, 81–109.

Kauhaniemi, M., J. Kukkonen, J. Härkonen, J. Nikmo, L. Kangas, G. Omstedt, M. Ketzel, A. Kousa, M. Haakana and A. Karppinen, 2011: Evaluation of a road dust suspension model for predicting the concentrations of PM10 in a street canyon. *Atmos. Environ.*, **45 (22)**, 3646–3654, doi:10.1016/j.atmosenv.2011.04.055.

Kikuchi, A., N. Hatay, A. Mochida, H. Yoshino, Y. Tabata, H. Watanabe and Y. Jyunimura, 2007: Field study of the influence of roadside trees and moving automobiles on turbulent diffusion of air pollutants and thermal environment in urban street canyons. *6th International Conference on Indoor Air Quality, Ventilation and Energy Conservation in Buildings*.

Kokkola, H., H. Korhonen, K. E. J. Lehtinen, R. Makkonen, A. Asmi, S. Järvenoja, T. Anttila, A.-I. Partanen, M. Kulmala, H. Järvinen, A. Laaksonen and V.-M. Kerminen, 2008: SALSA - a Sectional Aerosol module for Large Scale Applications. *Atmospheric Chemistry and Physics*, **8 (9)**, 2469–2483, URL https://hal.archives-ouvertes.fr/hal-00296541.

Kupiainen, K., L. Pirjola, R. Ritola, A. Stojiljkovic and A. Malinen, 2013: Talvirenkaiden pölypäästöt ja eri katupölylähteiden osuudet kadunvarrella kerätyissä hiukkasnäytteissä. *HSY:n julkaisuja*, in Finnish.

Kurppa, M., A. Hellsten, P. Roldin, H. Kokkola, J. Tonttila, M. Auvinen, C. Kent, P. Kumar, B. Maronga and L. Järvi, 2019: Implementation of the sectional aerosol module SALSA2.0 into the PALM model system 6.0: model development and first evaluation. *Geoscientific Model Development*, **12 (4)**, 1403–1422, doi:10.5194/gmd-12-1403-2019, URL https://www.geosci-model-dev.net/12/1403/2019/.

Leschziner, M., 2015: *Statistical Turbulence Modelling for Fluid Dynamics — Demystified*. Imperial College Press, doi:10.1142/p997, URL https://www.worldscientific.com/doi/abs/10.1142/p997, https://www.worldscientific.com/doi/pdf/10.1142/p997.

Letzel, M. O., M. Krane and S. Raasch, 2008: High resolution urban large-eddy simulation studies from street canyon to neighbourhood scale. *Atmospheric Environment*, **42 (38)**, 8770 – 8784, doi:https://doi.org/10.1016/j.atmosenv.2008.08.001, URL http://www.sciencedirect.com/science/article/pii/S1352231008007036.

Lietzke, B. and R. Vogt, 2013: Variability of co2 concentrations and fluxes in and above an urban street canyon. *Atmospheric Environment*, **74**, 60 – 72, doi:https://doi.org/10.1016/j.atmosenv.2013.03.030, URL http://www.sciencedirect.com/science/article/pii/S1352231013002069.

Locke, D., L. Roman and C. Murphy-Dunning, 2015: Why opt-in to a planting program? long-term residents value street tree aesthetics. *Arboriculture & Urban Forestry*, **41**, 324–333.

Macdonald, R. W., R. F. Griffiths and D. J. Hall, 1998: An improved method for the estimation of surface roughness of obstacle arrays. *Atmospheric Environment*, **32 (11)**, 1857–1864, doi:https://doi.org/10.1016/S1352-2310(97)00403-2, URL http://www.sciencedirect.com/science/article/pii/S1352231097004032.

Manisalidis, I., E. Stavropoulou, A. Stavropoulos and E. Bezirtzoglou, 2020: Environmental and health impacts of air pollution: A review. *Frontiers in public health*, **8**, 14–14, doi:10.3389/fpubh.2020.00014, URL https://pubmed.ncbi.nlm.nih.gov/32154200.

Markkanen, T., Ü. Rannik, B. Marcolla, A. Cescatti and T. Vesala, 2003: Footprints and fetches for fluxes over forest canopies with varying structure and density. *Boundary-Layer Meteorology*, **106 (3)**, 437–459, doi:10.1023/A:1021261606719, URL https://doi.org/10.1023/A:1021261606719.

Maronga, B., and Coauthors, 2020: Overview of the palm model system 6.0. *Geoscientific Model Development*, **13 (3)**, 1335–1372, doi:10.5194/gmd-13-1335-2020, URL https://www.geosci-model-dev.net/13/1335/2020/.

Ministry of the Environment, 2019: National air pollution control programme 2030. *Publications of the Ministry of the Environment*.

Moeng, C.-H. and J. C. Wyngaard, 1988: Spectral analysis of large-eddy simulations of the convective boundary layer. *Journal of the Atmospheric Sciences*, **45 (23)**, 3573–3587, doi:10.1175/1520-0469(1988)045<3573:SAOLES>2.0.CO;2, URL https://doi.org/10.1175/1520-0469(1988)045<3573:SAOLES>2.0.CO;2.

Mulhearn, P. J., 1978: Turbulent flow over a periodic rough surface. *The Physics of Fluids*, **21 (7)**, 1113–1115, doi:10.1063/1.862350, URL https://aip.scitation.org/doi/abs/10.1063/1.862350, https://aip.scitation.org/doi/pdf/10.1063/1.862350.

Munters, W., C. Meneveau and J. Meyers, 2016: Shifted periodic boundary conditions for simulations of wall-bounded turbulent flows. *Physics of Fluids*, **28 (2)**, 025 112, doi:10.1063/1.4941912, URL https://doi.org/10.1063/1.4941912.

Murphy, A. D., 2011: *Computational Fluid Dynamics : Theory, Analysis, and Applications*. Mechanical Engineering Theory and Applications, Nova Science Publishers, Inc.

Oke, T., 1988: Street design and urban canopy layer climate. *Energy and Buildings*, **11 (1)**, 103 – 113, doi:https://doi.org/10.1016/0378-7788(88)90026-6, URL http://www.sciencedirect.com/science/article/pii/0378778888900266.

Oke, T. R., G. Mills, A. Christen and J. A. Voogt, 2017: *Urban Climates*. Cambridge University Press, doi:10.1017/9781139016476.

O'Loughlin, E. M. and V. S. S. Annambhotla, 1969: Flow phenomena near rough boundaries. *Journal of Hydraulic Research*, **7 (2)**, 231–250, doi:10.1080/00221686909500265, URL https://doi.org/10.1080/00221686909500265, https://doi.org/10.1080/00221686909500265.

O'Neill, J., X.-M. Cai and R. Kinnersley, 2016: Stochastic backscatter modelling for the prediction of pollutant removal from an urban street canyon: A large-eddy simulation. *Atmospheric Environment*, **142**, 9 – 18, doi:https://doi.org/10.1016/j.atmosenv.2016.07.024, URL http://www.sciencedirect.com/science/article/pii/S135223101630543X.

Pakkanen, T. A., V.-M. Kerminen, C. H. Korhonen, R. E. Hillamo, P. Aarnio, T. Koskentalo and W. Maenhaut, 2001: Urban and rural ultrafine (PM0.1) particles in the helsinki area. *Atmospheric Environment*, **35 (27)**, 4593 – 4607, doi:https://doi.org/10.1016/S1352-2310(01)00167-4, URL http://www.sciencedirect.com/science/article/pii/S1352231001001674.

PALM technical documentation, 2020: *PALM technical documentation*. Institut für Meteorologie und Klimatologie, Gottfried Wilhelm Leibniz Universität Hannover, URL https://palm.muk.uni-hannover.de/trac/wiki/doc/tec, last access 4th of March 2020.

Poggi, D., A. Porporato, L. Ridolfi, J. D. Albertson and G. G. Katul, 2004: The effect of vegetation density on canopy sub-layer turbulence. *Boundary-Layer Meteorology*, **111 (3)**, 565–587, doi:10.1023/B:BOUN.0000016576.05621.73, URL https://doi.org/10.1023/B:BOUN.0000016576.05621.73.

Pope, S. B., 2000: *Turbulent Flows*. Cambridge University Press, doi:10.1017/CBO9780511840531.

Raupach, M. R., R. A. Antonia and S. Rajagopalan, 1991: Rough-Wall Turbulent Boundary Layers. *Applied Mechanics Reviews*, **44 (1)**, 1–25, doi:10.1115/1.

3119492, URL https://doi.org/10.1115/1.3119492, https://asmedigitalcollection.asme.org/appliedmechanicsreviews/article-pdf/44/1/1/5435787/1_1.pdf.

Raupach, M. R., P. A. Coppin and B. J. Legg, 1986: Experiments on scalar dispersion within a model plant canopy part i: The turbulence structure. *Boundary-Layer Meteorology*, **35 (1)**, 21–52, doi:10.1007/BF00117300, URL https://doi.org/10.1007/BF00117300.

Raupach, M. R., J. J. Finnigan and Y. Brunei, 1996: Coherent eddies and turbulence in vegetation canopies: The mixing-layer analogy. *Boundary-Layer Meteorology*, **78 (3)**, 351–382, doi:10.1007/BF00120941, URL https://doi.org/10.1007/BF00120941.

Raupach, M. R., A. S. Thom and I. Edwards, 1980: A wind-tunnel study of turbulent flow close to regularly arrayed rough surfaces. *Boundary-Layer Meteorology*, **18 (4)**, 373–397, doi:10.1007/BF00119495, URL https://doi.org/10.1007/BF00119495.

Rencher, A. C. and W. F. Christensen, 2012: *Methods of Multivariate Analysis*. John Wiley & Sons, Incorporated, Somerset, UNITED STATES.

Salizzoni, P., L. Soulhac and P. Mejean, 2009: Street canyon ventilation and atmospheric turbulence. *Atmospheric Environment*, **43 (32)**, 5056–5067, doi:https://doi.org/10.1016/j.atmosenv.2009.06.045, URL http://www.sciencedirect.com/science/article/pii/S1352231009005585.

Salmond, J., D. Williams, G. Laing, S. Kingham, K. Dirks, I. Longley and G. Henshaw, 2013: The influence of vegetation on the horizontal and vertical distribution of pollutants in a street canyon. *Science of The Total Environment*, **443**, 287 – 298, doi:https://doi.org/10.1016/j.scitotenv.2012.10.101, URL http://www.sciencedirect.com/science/article/pii/S0048969712014015.

Shaw, R. H. and U. Schumann, 1992: Large-eddy simulation of turbulent flow above and within a forest. *Boundary-Layer Meteorology*, **61 (1)**, 47–64, doi:10.1007/BF02033994, URL https://doi.org/10.1007/BF02033994.

Shaw, R. H., J. Tavangar and D. P. Ward, 1983: Structure of the reynolds stress in a canopy layer. *Journal of Climate and Applied Meteorology*, **22 (11)**, 1922–1931, doi:101175/1520-0450(1983)022<1922:SOTRSI>2.0.CO;2, URL https://doi.org/10.1175/1520-0450(1983)022<1922:SOTRSI>2.0.CO;2, https://doi.org/10.1175/1520-0450(1983)022<1922:SOTRSI>2.0.CO;2.

Stewart, I. D. and T. R. Oke, 2012: Local climate zones for urban temperature studies. *Bulletin of the American Meteorological Society*, **93 (12)**, 1879–1900, doi:10.1175/BAMS-D-11-00019.1, URL https://doi.org/10.1175/BAMS-D-11-00019.1.

Stull, R. B., 1988: *An Introduction To Boundary Layer Meteorology*. Kluwer Academic Publishers.

Tanhuanpää, T., M. Vastaranta, V. Kankare, M. Holopainen, J. Hyyppä, H. Hyyppä, P. Alho and J. Raisio, 2014: Mapping of urban roadside trees – a case study in the tree register update process in helsinki city. *Urban Forestry & Urban Greening*, **13 (3)**, 562 – 570, doi:https://doi.org/10.1016/j.ufug.2014.03.005, URL http://www.sciencedirect.com/science/article/pii/S1618866714000314.

Tecer, L. H., O. Alagha, F. Karaca, G. Tuncel and N. Eldes, 2008: Particulate matter (PM2.5, PM10-2.5, and PM10) and children's hospital admissions for asthma and respiratory diseases: A bidirectional case-crossover study. *Journal of Toxicology and Environmental Health, Part A*, **71 (8)**, 512–520, doi:10.1080/15287390801907459, URL https://doi.org/10.1080/15287390801907459, pMID: 18338286, https://doi.org/10.1080/15287390801907459.

Tennekes, H. and J. L. Lumley, 1972: *A first course in turbulence*. The Massachusetts Institute of Technology.

Terzano, C., F. Di Stefano, V. Conti, E. Graziani and A. Petroianni, 2010: Air pollution ultrafine particles: Toxicity beyond the lung. *European Review for Medical and Pharmacological Sciences*, **14 (10)**, 809–821.

Thom, A. S., 1972: Momentum, mass and heat exchange of vegetation. *Quarterly Journal of the Royal Meteorological Society*, **98 (415)**, 124–134, doi:10.1002/qj.49709841510, URL https://rmets.onlinelibrary.wiley.com/doi/abs/10.1002/qj.49709841510, https://rmets.onlinelibrary.wiley.com/doi/pdf/10.1002/qj.49709841510.

Timonen, S. and P. Kauppinen, 2008: Mycorrhizal colonisation patterns of tilia trees in street, nursery and forest habitats in southern finland. *Urban Forestry & Urban Greening*, **7 (4)**, 265 – 276, doi:https://doi.org/10.1016/j.ufug.2008.08.001, URL http://www.sciencedirect.com/science/article/pii/S1618866708000381.

Tominaga, Y. and T. Stathopoulos, 2010: Numerical simulation of dispersion around an isolated cubic building: Model evaluation of rans and les. *Building and Environment*, **45 (10)**, 2231 – 2239, doi:https://doi.org/10.1016/j.buildenv.2010.04.004, URL http://www.sciencedirect.com/science/article/pii/S0360132310001113.

Tominaga, Y. and T. Stathopoulos, 2011: Cfd modeling of pollution dispersion in a street canyon: Comparison between les and rans. *Journal of Wind Engineering and Industrial Aerodynamics*, **99 (4)**, 340 – 348, doi:https://doi.org/10.1016/j.jweia.2010.12.005, URL http://www.sciencedirect.com/science/article/pii/S0167610510001388, the Fifth International Symposium on Computational Wind Engineering.

Tritton, D. J., 1988: *Physical Fluid Dynamics*. Oxford University Press.

Vogel, S., 1989: Drag and Reconfiguration of Broad Leaves in High Winds. *Journal of Experimental Botany*, **40 (8)**, 941–948, doi:10.1093/jxb/40.8.941, URL https://doi.org/10.1093/jxb/40.8.941, https://academic.oup.com/jxb/article-pdf/40/8/941/1661209/40-8-941.pdf.

Vos, P. E., B. Maiheu, J. Vankerkom and S. Janssen, 2013: Improving local air quality in cities: To tree or not to tree? *Environmental Pollution*, **183**, 113 – 122, doi:https://doi.org/10.1016/j.envpol.2012.10.021, URL http://www.sciencedirect.com/science/article/pii/S0269749112004605, selected Papers from Urban Environmental Pollution 2012.

VTT, 2018a: ALIISA vehicle fleet model. Technical Research Centre of Finland Ltd. URL http://lipasto.vtt.fi/en/aliisa/index.htm, last access 17 September 2018.

VTT, 2018b: LIPASTO - calculation system for traffic exhaust emissions and energy use in Finland. Technical Research Centre of Finland Ltd. URL http://lipasto.vtt.fi/en/index.htm, last access 17 September 2018.

Walton, A. and A. Cheng, 2002: Large-eddy simulation of pollution dispersion in an urban street canyon—part ii: idealised canyon simulation. *Atmospheric Environment*, **36 (22)**, 3615 – 3627, doi:https://doi.org/10.1016/S1352-2310(02)00260-1, URL http://www.sciencedirect.com/science/article/pii/S1352231002002601.

Wedi, N., K. Yessad and A. Untch, 2009: The non-hydrostatic global IFS/ARPEGE model: model formulation and testing. *ECMWF Technical Memoranda*, 34, doi:10.21957/tl4f0ao4t, URL https://www.ecmwf.int/node/13031.

WHO, 2006: WHO Air quality guidelines for particulate matter, ozone, nitrogen dioxide and sulfur dioxide.

Wicker, L. J. and W. C. Skamarock, 2002: Time-splitting methods for elastic models using forward time schemes. *Monthly Weather Review*, **130 (8)**, 2088–2097, doi:10.1175/1520-0493(2002)130<2088:TSMFEM>2.0.CO;2, URL https://doi.org/10.1175/1520-0493(2002)130<2088:TSMFEM>2.0.CO;2.

World Health Assembly, 2015: Health and the environment: addressing the health impact of air pollution. *Draft resolution proposed by the delegations of Albania, Chile, Colombia, France, Germany, Monaco, Norway, Panama, Sweden, Switzerland, Ukraine, United States of America, Uruguay and Zambia.*

Xue, J., Y. Li, X. Wang, T. D. Durbin, K. C. Johnson, G. Karavalakis, A. Asa-Awuku, M. Villela, D. Quiros, S. Hu, T. Huai, A. Ayala and H. S. Jung, 2015: Comparison of vehicle exhaust particle size distributions measured by smps and eeps dur-

ing steady-state conditions. *Aerosol Science and Technology*, **49 (10)**, 984–996, doi:10.1080/02786826.2015.1088146, URL https://doi.org/10.1080/02786826.2015.1088146, https://doi.org/10.1080/02786826.2015.1088146.

Yazid, A. W. M., N. A. C. Sidik, S. M. Salim and K. M. Saqr, 2014: A review on the flow structure and pollutant dispersion in urban street canyons for urban planning strategies. *Simulation*, **90 (8)**, 892–916, doi:10.1177/0037549714528046, URL https://doi.org/10.1177/0037549714528046.

Zhang, Y., C. Seigneur, J. H. Seinfeld, M. Z. Jacobson and F. S. Binkowski, 1999: Simulation of aerosol dynamics: A comparative review of algorithms used in air quality models. *Aerosol Sci. Tech.*, **31 (6)**, 487–514, doi:10.1080/027868299304039.

Zikanov, O., 2010: *Essential Computational Fluid Dynamics*. John Wiley & Sons, Incorporated, New York, United States.